CISSIR: Beam Codebooks with Self-Interference Reduction Guarantees for Integrated Sensing and Communication Beyond 5G

Rodrigo Hernangómez, *Member, IEEE,* Jochen Fink, *Member, IEEE,*
Renato Luís Garrido Cavalcante, *Member, IEEE,* and Sławomir Stańczak, *Senior Member, IEEE*

arXiv:2502.10371v3 [eess.SP] 22 Oct 2025

***Abstract*—We propose a beam codebook design for integrated sensing and communication (ISAC) that reduces self-interference (SI) to alleviate analog distortion. Our optimization framework, which considers either tapered beamforming or phased arrays for both analog and hybrid schemes, modifies given reference codebooks such that a certain SI power level is achieved. In contrast to other low-SI codebooks, which often rely on hardly interpretable optimization parameters, we provide design guidelines to obtain sensing performance guarantees by deriving analytical bounds on saturation and analog-to-digital quantization in relation to the multipath SI level. By selecting standard reference codebooks in our simulations, we show how our method substantially improves the signal-to-noise ratio for sensing with little impact on 5G-NR communication.**

***Index Terms*—Integrated sensing and communication, beamforming, phased arrays, self-interference**

I. Introduction

NEXT-GENERATION mobile networks are expected to incorporate sensing capabilities as an additional service [1]. To this aim, the paradigm of integrated sensing and communication (ISAC) is being actively investigated, and ISAC's many challenges and opportunities are rapidly unfolding as a result [2]–[4].

Self-interference (SI) has been identified as one such ISAC challenge, principally, but not only, in so-called monostatic setups with co-located transmission (TX) and reception (RX) sensing systems [4]–[7]. Self-interference is sometimes addressed by adopting radar-centric ISAC waveforms [8], for which, similarly as for conventional radar, simple analog circuitry can isolate the RX echoes from the TX signals on the time-frequency plane [9]. This principle, although proven useful even for joint design schemes [10], cannot be generally applied to the communication-centric waveforms that mobile networks usually employ, as these are typically dense in time and frequency [6], [7]. As a result, SI produces an unwanted signal contribution at communication-centric ISAC receivers, causing adverse effects along the processing chain: saturation at the RX antenna, desensitization at the analog-to-digital converter (ADC), or signal masking in the digital baseband [11], [12]. Here, the former stages are critical, as they may introduce nonlinear distortion. For this reason, a cascaded approach is often adopted, such that different SI thresholds are attained at each analog stage to avoid distortion, and the residual SI is canceled in the digital domain [9], [11].

Many strategies to reduce SI for communication waveforms have been studied in the literature, often through the lens of the full-duplex paradigm [6], [7]. This includes passive antenna elements [12], [13], active cancelers [11], [14], beamforming [15]–[21], or intelligent metasurfaces [22]; a comprehensive review can be found in [23]. While most techniques require drastic innovations in mobile networks and standards, SI-reducing beamforming may leverage the existing multiple-input multiple-output (MIMO) capabilities in the 5G new radio (NR) standard [24] to enable ISAC upon current infrastructure. Analog [15]–[18] and hybrid [19], [20] architectures represent a natural choice here, since digital RX beamforming fails to address all effects happening before the ADC [21].

Regarding beamforming and MIMO processing, 5G NR often resorts to predefined beam codebooks to reduce channel feedback overhead [24]–[26]. In this vein, the authors of LoneSTAR [17] and of [18] have proposed design methods for codebooks that achieve considerably low SI. These methods, however, rely on hyperparameter tuning and heuristic optimization, and they are devised with the assumption of flat-fading SI channels. In contrast to this, radio measurements and industrial applications often deal with multipath SI, whereby strong clutter reflections are as relevant as direct antenna coupling despite the longer propagation path [27]–[29].

In this paper, we propose a principled low-SI beamforming design method for ISAC, which yields codebooks with integral split for self-interference reduction (CISSIR)[1]. The main contributions can be summarized as follows:

- We adopt a multipath MIMO SI model for ISAC beamforming, which, to the best of our knowledge, had not been addressed yet in the literature. Our model covers both analog and hybrid beam codebooks, while considering realistic ADC sampling.
- We devise a simple optimization framework to design codebooks based on either tapered beamforming, using matrix decomposition, or phased arrays via semidefinite programming (SDP) [30]. In contrast to the state of the art [17], [18], our framework parametrizes the SI level incurred by the TX and RX codebooks, which we design independently from each other by splitting the SI channel.

[1]Pronounced like "scissor".

©2025 IEEE. Personal use of this material is permitted. Permission from IEEE must be obtained for all other uses, in any current or future media, including reprinting / republishing this material for advertising or promotional purposes, creating new collective works, for resale or redistribution to servers or lists, or reuse of any copyrighted component of this work in other works.

- Furthermore, we derive novel analytical bounds that allow us to select optimization parameters systematically to meet sensing quality criteria, thus endowing CISSIR with feasibility and performance guarantees. More specifically, the derived bounds relate the SI level with the ADC quantization error and the RX saturation. Our simulations confirm the superior performance of CISSIR over the LoneSTAR codebook [17] according to said criteria, while hinting at the compatibility of our method with the 5G-NR standard via link-level results.
- Lastly, we have based our code on popular open-source libraries like Sionna™ [31] and CVXPY [32], and we have made it publicly available for reproducibility[2].

The remainder of this paper is organized as follows: Section II introduces the system model and the optimization problem to design SI-reduced beam codebooks for ISAC. Section III presents the proposed solution, based on the TX-RX split of the multipath MIMO SI channel. Section IV establishes the analytical bounds of our scheme, providing parameter-selection guidelines to meet given sensing constraints. Section V compares CISSIR to LoneSTAR [17] and to customary 5G-NR codebooks [24], [25], via ray-tracing and link-level simulations. Finally, Section VI delivers some concluding remarks and a possible outlook of this work.

A. Notation and preliminaries

We define $[N] \coloneqq \{1, 2, \dots, N\}$ for a positive integer N. For $z \in \mathbb{C}$, we indicate its real and imaginary parts as $\Re(z)$ and $\Im(z)$, and its conjugate as $z^* = \Re(z) - j\Im(z)$ with $j = \sqrt{-1}$.

We write $\mathcal{CN}(0, \sigma^2)$ to denote the zero-mean complex normal distribution with variance σ^2, and $\mathcal{U}(a, b)$ for the uniform distribution in $[a, b]$. The expected value of a random variable X is written as $\mathbb{E}[X]$.

Uppercase bold letters represent matrices $\mathbf{V} \in \mathbb{C}^{M\times N}$, with subindexed lowercase bold letters indicating their column vectors, $\mathbf{V} = [\mathbf{v}_1, \dots, \mathbf{v}_N]$, $(\forall n \in [N])\ \mathbf{v}_n \in \mathbb{C}^M$. We write the convolution of functions $f : \mathbb{R} \to \mathbb{C}$ and $g : \mathbb{R} \to \mathbb{C}$ as $f * g$. For $p \in [1, \infty]$, the p-norm for vectors $\mathbf{v} \in \mathbb{C}^M$ is written as $\|\mathbf{v}\|_p$, whereas $|f|_p$ denotes the p-norm for functions $(\forall a, b \in \mathbb{R}$ and $a < b)$ $f : [a, b] \to \mathbb{C}$, to avoid confusion. Moreover, $\|\mathbf{M}\|_{\mathrm{F}}$, $\|\mathbf{M}\|_2$, and $\|\mathbf{M}\|_*$ indicate the Frobenius, spectral, and nuclear norms, respectively, of $\mathbf{M} \in \mathbb{C}^{M\times N}$. For any matrix $\mathbf{A} \in \mathbb{C}^{M\times N}$, we write its transpose as $\mathbf{A}^{\mathsf{T}}$ and its Hermitian transpose as $\mathbf{A}^{\mathsf{H}} = (\mathbf{A}^*)^{\mathsf{T}}$. For a matrix-valued function $\mathbf{H} : \mathbb{R} \to \mathbb{C}^{M\times N}$, $\mathbf{c} \in \mathbb{C}^M$, and $\mathbf{w} \in \mathbb{C}^N$, $(\mathbf{c}^{\mathsf{H}}\mathbf{H}\mathbf{w})(t)$ stands for the function $t \mapsto \mathbf{c}^{\mathsf{H}}\mathbf{H}(t)\mathbf{w}$, and the integral of $\mathbf{H}(t)$ is understood entry-wise, i.e. $(\forall n \in [N]\,, \forall m \in [M])$:

$$\left[\int_{t_0}^{t_1} \mathbf{H}(t)\, dt\right]_{m,n} = \int_{t_0}^{t_1} [\mathbf{H}(t)]_{m,n}\, dt\,.$$

For any pair of Hermitian matrices $\mathbf{A}, \mathbf{B} \in \mathbb{S}^M \coloneqq \{\mathbf{X} \in \mathbb{C}^{M\times M} | \, \mathbf{X} = \mathbf{X}^{\mathsf{H}}\}$, we consider the inner product $\langle \mathbf{A}, \mathbf{B}\rangle \coloneqq \mathrm{tr}(\mathbf{B}^{\mathsf{H}}\mathbf{A}) = \mathrm{tr}(\mathbf{B}\mathbf{A}) \in \mathbb{R}$. We denote by $\mathbb{S}^M_+ \subset \mathbb{S}^M$ the $M \times M$ positive semidefinite cone, which induces the partial order $(\forall \mathbf{A}, \mathbf{B} \in \mathbb{S}^M)$ $\mathbf{A} \succcurlyeq \mathbf{B} \iff \mathbf{A} - \mathbf{B} \in \mathbb{S}^M_+$.

[2]Code available at github.com/rodrihgh/cissir

II. System model and problem formulation

A. System model

We consider a hybrid-beamforming MIMO system with N TX antennas and $L < N$ TX radio frequency (RF) chains, as depicted in Fig. 1. For a given time slot of length T, the TX RF chains are fed with L time-continuous signals, which we write in vector form $(\forall t \in [0, T])$ as $\mathbf{x}(t) \coloneqq [x_1(t), \dots, x_L(t)]$ with $(\forall \ell \in [L])$ $x_\ell : [0, T] \to \mathbb{C}$.

The signals in $\mathbf{x}(t)$ carry user data and are transmitted according to L selected beamforming vectors out of $L' \geq L$ columns from a given TX codebook matrix $\mathbf{W} \in \mathbb{C}^{N\times L'}$. The TX chain accepts any suitable existing mechanism for beam selection, denoted as the mapping $\jmath : [L] \to [L']$. That is, $(\forall \ell \in [L])$ the beamformer $\mathbf{w}_{\jmath(\ell)}$ is applied to $x_\ell(t)$.

Moreover, the system is equipped with an RX sniffer [33] dedicated to radar sensing, whereas time-division duplex (TDD) communication is assumed in accordance with 5G frequency range 2 (FR2) [24]. The RX sniffer has M antennas and K RF chains, such that $(\forall k \in [K])$ the k-th RX signal is beamformed by $\mathbf{c}_{\imath(k)}$, a vector selected from the $K' \geq K$ columns in the RX codebook $\mathbf{C} \in \mathbb{C}^{M\times K'}$. The RX beam mapping $\imath : [K] \to [K']$ is envisioned to match the TX beam directions given by $\jmath$ to maximize the RX echo power [20].

The TX and RX codebooks are restricted to the feasibility sets $\mathcal{W}^{L'}$ and $\mathcal{C}^{K'}$, i.e.:

$$\mathbf{W} \in \mathcal{W}^{L'} \coloneqq \left\{\mathbf{W} \in \mathbb{C}^{N\times L'} \middle| (\forall \ell \in [L'])\ \mathbf{w}_\ell \in \mathcal{W}\right\},$$
$$\mathbf{C} \in \mathcal{C}^{K'} \coloneqq \left\{\mathbf{C} \in \mathbb{C}^{M\times K'} \middle| (\forall k \in [K'])\ \mathbf{c}_k \in \mathcal{C}\right\},$$

where $\mathcal{W} \in \{\mathcal{W}_\triangleright, \mathcal{W}_\oslash\}$ and $\mathcal{C} \in \{\mathcal{C}_\triangleright, \mathcal{C}_\oslash\}$ express constraints for either tapered beamforming or phased arrays, the two most common array technologies. In the tapered case, the codebook columns are only subject to unit power:

$$\mathcal{W}_\triangleright \coloneqq \left\{\mathbf{w} \in \mathbb{C}^N \middle| \|\mathbf{w}\|_2 = 1\right\}, \mathcal{C}_\triangleright \coloneqq \left\{\mathbf{c} \in \mathbb{C}^M \middle| \|\mathbf{c}\|_2 = 1\right\}. \tag{1}$$

On the other hand, for phased arrays we have

$$\mathcal{W}_\oslash \coloneqq \left\{\mathbf{w} \in \mathbb{C}^N \,\middle|\, (\forall n \in [N])\ |[\mathbf{w}]_n| = 1/\sqrt{N}\right\},$$
$$\mathcal{C}_\oslash \coloneqq \left\{\mathbf{c} \in \mathbb{C}^M \,\middle|\, (\forall m \in [M])\ |[\mathbf{c}]_m| = 1/\sqrt{M}\right\}.$$

We note that $\mathcal{W}_\oslash \subset \mathcal{W}_\triangleright$ and $\mathcal{C}_\oslash \subset \mathcal{C}_\triangleright$, i.e., beam unit power is assumed for both beamforming variants.

The signals in $\mathbf{x}(t)$ impinge on the RX sniffer over a MIMO channel $\mathbf{H} : [0, T_\mathrm{c}] \to \mathbb{C}^{M\times N}$ with maximum delay T_c, which we write $(\forall t \in [0, T_\mathrm{c}], \forall m \in [M], \forall n \in [N])$ as:

$$\mathbf{H}(t) \coloneqq \begin{bmatrix} h_{1,1}(t) & \dots & h_{1,N}(t) \\ \vdots & \ddots & \vdots \\ h_{M,1}(t) & \dots & h_{M,N}(t) \end{bmatrix},\ h_{m,n} : [0, T_\mathrm{c}] \to \mathbb{C}\,. \tag{2}$$

Furthermore, we assume $\mathbf{H}(t)$ to be the superimposition of the unknown radar channel $\mathbf{H}_\mathrm{r} : [0, T_\mathrm{c}] \to \mathbb{C}^{M\times N}$ and the SI channel $\mathbf{S} : [0, T_\mathrm{c}] \to \mathbb{C}^{M\times N}$:

$$(\forall t \in [0, T_\mathrm{c}])\ \mathbf{H}(t) = \mathbf{H}_\mathrm{r}(t) + \mathbf{S}(t)\,.$$

We assume $\mathbf{S}(t)$ is known through estimation procedures like those described in [17], whereby the SI is separated from the

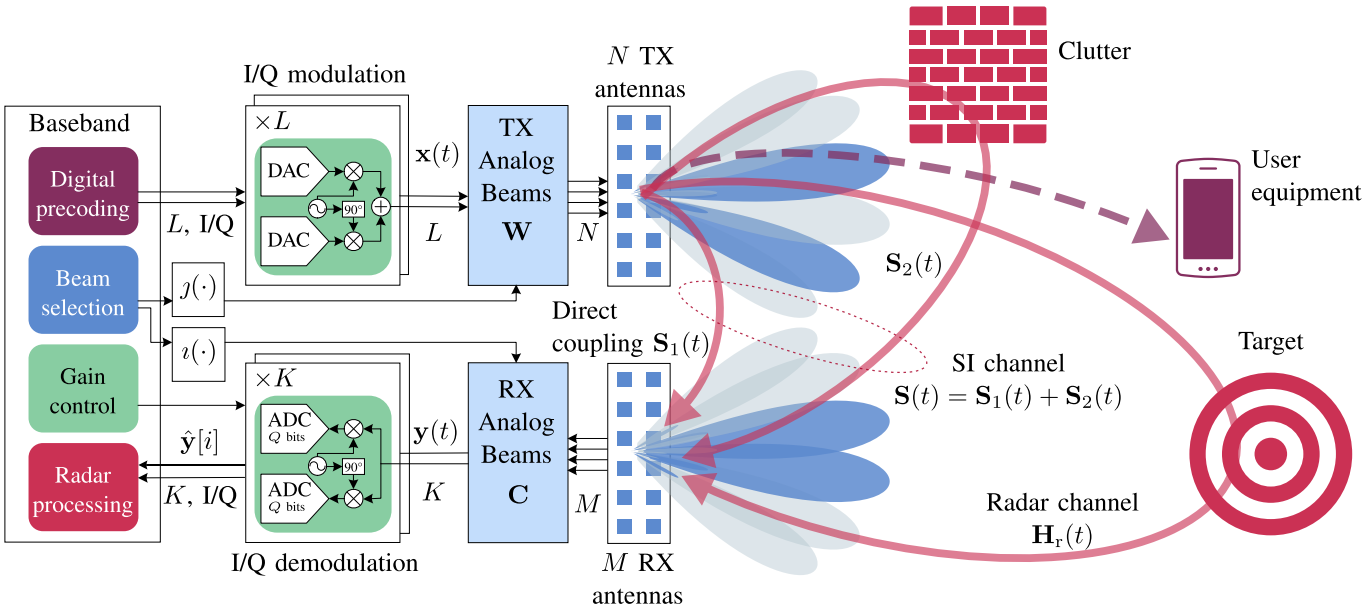


Fig. 1. System model: ISAC beam codebooks in the face of multipath self-interference (SI). Amplifiers and filters are omitted for simplicity.

radar channel in the delay-Doppler domain by exploiting the short-range and static nature of $\mathbf{S}(t)$ [27], [34]. While our analysis holds for arbitrary bounded matrix-valued functions, we choose to model $\mathbf{S}(t) = \sum_{d=1}^{D} \mathbf{S}_d(t)$ as a sum of D paths. This choice, motivated by the available measurements in the literature [28], allows us to differentiate between direct antenna coupling and clutter reflections ($\mathbf{S}_1(t)$ and $\mathbf{S}_2(t)$ in Fig. 1) for an easier comparison with single-path approaches. All entries in $\mathbf{H}_{\mathrm{r}}(t)$ and $\mathbf{S}(t)$ are functions with domain in $[0, T_{\mathrm{c}}]$, similarly to the entries of $\mathbf{H}(t)$ in (2).

The RX signals are expressed in vector form as $\mathbf{y}(t)$:

$$(\forall t \in [0, T + T_{\mathrm{c}}]) \quad \mathbf{y}(t) = [y_1(t), \dots, y_K(t)]^\top, \text{ where}$$
$$(\forall k \in [K]) \quad y_k(t) = \sum_{\ell=1}^{L} \left(\left(\mathbf{c}_{\imath(k)}^{\mathsf{H}} \mathbf{H}\, \mathbf{w}_{\jmath(\ell)} \right) * x_\ell \right)(t). \tag{3}$$

For all $k \in [K]$, two ADCs sample the in-phase/quadrature (I/Q) components of $y_k(t)$ at the rate $1/T_{\mathrm{S}}$ with Q quantization bits each, yielding the following RX digital sensing signal ($\forall i \in \{0, 1, \dots, \lfloor (T + T_{\mathrm{c}})/T_{\mathrm{S}} \rfloor\}$):

$$\hat{\mathbf{y}}[i] = [\hat{y}_1[i], \dots, \hat{y}_K[i]]^\top,$$
$$(\forall k \in [K]) \quad \hat{y}_k[i] \coloneqq y_k(iT_{\mathrm{S}}) + v_k[i] + u_k[i]. \tag{4}$$

In (4), $v_k[i] \sim \mathcal{CN}(0, \sigma_{\mathrm{T}}^2)$ is a sample of independent identically distributed (i.i.d.) thermal noise, whereas $u_k[i]$ is an independent sample of complex quantization noise. The latter is described in more detail in Section IV.

B. The optimization problem

Given a pair of TX/RX beam codebooks $\mathbf{A} \in \mathcal{W}^{L'}$ and $\mathbf{B} \in \mathcal{C}^{K'}$, which we assume optimal for TDD codebook-based communication, we aim to derive a codebook pair $(\mathbf{W}, \mathbf{C})$ that guarantees a certain sensing quality in the presence of SI. We assess sensing quality via the signal-to-noise ratio (SNR), which directly determines detection and estimation performance [9]. In practice, SI and SNR are linked through the quantization noise $\sigma_{\mathrm{Q}}^2 \coloneqq \mathbb{E}[|u_k[i]|^2]$, as we show in Section IV. In particular, Lemma 1 therein allows to bound σ_{Q}, up to a scaling factor, by the *maximum SI (max. SI)* $\mathfrak{m}_{\mathbf{S}}(\mathbf{C}, \mathbf{W})$, which we define for $\mathbf{S}(t)$ ($\forall\, \mathbf{C} \in \mathcal{C}^{K'}$, $\forall\, \mathbf{W} \in \mathcal{W}^{L'}$) as

$$\mathfrak{m}_{\mathbf{S}}(\mathbf{C}, \mathbf{W}) \coloneqq \max_{\substack{k \in [K'], \\ \ell \in [L']}} \int_0^{T_{\mathrm{c}}} \left| \mathbf{c}_k^{\mathsf{H}} \mathbf{S}(t) \mathbf{w}_\ell \right| \, dt\,. \tag{5}$$

Therefore, we choose to limit the SI-induced quantization noise by imposing a certain *target SI* $\varepsilon > 0$ such that $\mathfrak{m}_{\mathbf{S}}(\mathbf{C}, \mathbf{W}) \leq \varepsilon$. We note that (5) does not depend on the TX signal $\mathbf{x}(t)$ or the beam-selection mappings $\imath$ and $\jmath$, since these may be unknown during codebook design.

Moreover, we wish to optimize communication by minimizing σ_{tx}^2, the deviation of the ISAC TX codebook $\mathbf{W}$ from the communication-optimal codebook $\mathbf{A}$. We also aim to minimize the deviation σ_{rx}^2 between $\mathbf{B}$ and the RX codebook $\mathbf{C}$, which could be potentially used for standard TDD communication. Additionally, designing $(\mathbf{W}, \mathbf{C})$ close to $(\mathbf{A}, \mathbf{B})$ may improve the sensing SNR, since practical communication codebooks usually maximize the TX/RX gain across a grid of angular directions [24], [25]. In other words, σ_{tx}^2 and σ_{rx}^2 minimization tends to increase the numerator of $\mathrm{SNR} \propto \left| \mathbf{c}_{k_\theta}^{\mathsf{H}} \mathbf{b}_\theta \mathbf{a}_\theta^{\mathsf{H}} \mathbf{w}_{\ell_\theta} \right|^2$ for a target at the direction given by the steering vectors $\mathbf{a}_\theta \in \mathbb{C}^N$, $\mathbf{b}_\theta \in \mathbb{C}^M$, and for certain unknown beam indices $\ell_\theta \in [L']$, $k_\theta \in [K']$.

In line with the literature [17], [18], we compute σ_{tx}^2 and σ_{rx}^2 with the Frobenius norm, i.e.:

$$\sigma_{\mathrm{tx}}^2 \coloneqq \|\mathbf{W} - \mathbf{A}\|_{\mathrm{F}}^2 \,/\, \underbrace{\|\mathbf{A}\|_{\mathrm{F}}^2}_{=L'} = \frac{1}{L'} \sum_{\ell=1}^{L'} \|\mathbf{w}_\ell - \mathbf{a}_\ell\|_2^2\,,$$
$$\sigma_{\mathrm{rx}}^2 \coloneqq \|\mathbf{C} - \mathbf{B}\|_{\mathrm{F}}^2 \,/\, \underbrace{\|\mathbf{B}\|_{\mathrm{F}}^2}_{=K'} = \frac{1}{K'} \sum_{k=1}^{K'} \|\mathbf{c}_k - \mathbf{b}_k\|_2^2\,. \tag{6}$$

Hence, the design of $(\mathbf{W}, \mathbf{C})$ can be posed as the following optimization problem:

$$\underset{\mathbf{W}\in\mathcal{W}^{L'},\,\mathbf{C}\in\mathcal{C}^{K'}}{\text{minimize}} \ \|\mathbf{W}-\mathbf{A}\|_{\mathrm{F}}^2+\omega\,\|\mathbf{C}-\mathbf{B}\|_{\mathrm{F}}^2 \tag{7a}$$

$$\text{s.t.} \quad \mathfrak{m}_{\mathbf{S}}(\mathbf{C},\mathbf{W}) \le \varepsilon\,, \tag{7b}$$

with $\omega > 0$ a trade-off parameter between TX and RX codebook deviation. Problem (7) inverts the approach taken in [17], [18], where the (flat-fading) SI is minimized under a heuristically tuned maximum codebook deviation constraint $\sigma_{\mathrm{cb}}^2 \ge \max\{\sigma_{\mathrm{tx}}^2, \sigma_{\mathrm{rx}}^2\}$. In contrast to this, Problem (7) enables both the tuning of ε according to sensing metrics (cf. Section IV), and the mitigation of multipath SI, via $\mathfrak{m}_{\mathbf{S}}(\mathbf{C},\mathbf{W})$.

III. Proposed scheme

Problem (7) is nonconvex because of the constraint sets $\mathcal{C}^{K'}$ and $\mathcal{W}^{L'}$, and also due to the coupling of the codebooks $\mathbf{C}$ and $\mathbf{W}$ in $\mathfrak{m}_{\mathbf{S}}(\mathbf{C},\mathbf{W})$. In order to derive a more tractable problem, we propose a decoupling of $\mathbf{C}$ and $\mathbf{W}$. The resulting problem, albeit still nonconvex, can be solved optimally for the case of tapered beamforming and phased arrays, as we detail in Sections III-B–III-C.

As a preliminary step, we note that we can modify (7a), given the unit power constraint (1), to write Problem (7) in the following equivalent form:

$$\underset{\mathbf{W}\in\mathcal{W}^{L'},\,\mathbf{C}\in\mathcal{C}^{K'}}{\text{maximize}} \ \frac{1}{L'}\sum_{\ell=1}^{L'}\Re\left(\mathbf{a}_\ell^{\mathsf{H}}\mathbf{w}_\ell\right)+\frac{\omega}{K'}\sum_{k=1}^{K'}\Re\left(\mathbf{b}_k^{\mathsf{H}}\mathbf{c}_k\right) \tag{8}$$

$$\text{s.t.} \ \ (\forall k\in[K'],\forall \ell\in[L']) \quad \int_0^{T_{\mathrm{c}}}\left|\mathbf{c}_k^{\mathsf{H}}\mathbf{S}(t)\mathbf{w}_\ell\right|\,dt \le \varepsilon\,.$$

A. Problem decoupling

We propose an alternative to (8) that allows us to optimize the columns of $\mathbf{C}$ and $\mathbf{W}$ individually while $(\mathbf{C}, \mathbf{W})$ remains in the original feasible region. For this, we consider the following decomposition, which we refer to as *integral split*.

Definition 1 (Integral split)**.** We define the integral split of an SI channel $\mathbf{S}(t)$ as the matrices $\mathbf{G}_{\mathrm{tx}} \in \mathbb{S}_+^N$ and $\mathbf{G}_{\mathrm{rx}} \in \mathbb{S}_+^M$:

$$\mathbf{G}_{\mathrm{tx}} \coloneqq \int_0^{T_{\mathrm{c}}} \mathbf{V}_t\mathbf{\Sigma}_t\mathbf{V}_t^{\mathsf{H}}\,dt\,, \text{ and } \mathbf{G}_{\mathrm{rx}} \coloneqq \int_0^{T_{\mathrm{c}}} \mathbf{U}_t\mathbf{\Sigma}_t\mathbf{U}_t^{\mathsf{H}}\,dt\,,$$

where, for every $t \in [0, T_{\mathrm{c}}]$, $\mathbf{U}_t$, $\mathbf{\Sigma}_t$, and $\mathbf{V}_t^{\mathsf{H}}$ are given as a singular value decomposition (SVD) of $\mathbf{S}(t) = \mathbf{U}_t\mathbf{\Sigma}_t\mathbf{V}_t^{\mathsf{H}}$.

Proposition 1. *Let $\mathbf{G}_{\mathrm{tx}} \in \mathbb{S}_+^N$ and $\mathbf{G}_{\mathrm{rx}} \in \mathbb{S}_+^M$ be the integral split (see Definition 1) of $\mathbf{S}(t)$ in* (5)*, and consider the quantity $(\forall\,\mathbf{C}\in\mathcal{C}^{K'},\,\forall\,\mathbf{W}\in\mathcal{W}^{L'})$:*

$$\widehat{\mathfrak{m}}_{\mathbf{S}}(\mathbf{C},\mathbf{W}) \coloneqq \max_{k\in[K']}\sqrt{\mathbf{c}_k^{\mathsf{H}}\mathbf{G}_{\mathrm{rx}}\mathbf{c}_k}\max_{\ell\in[L']}\sqrt{\mathbf{w}_\ell^{\mathsf{H}}\mathbf{G}_{\mathrm{tx}}\mathbf{w}_\ell}\,.$$

Then, we have: $$\mathfrak{m}_{\mathbf{S}}(\mathbf{C},\mathbf{W}) \le \widehat{\mathfrak{m}}_{\mathbf{S}}(\mathbf{C},\mathbf{W})\,. \tag{9}$$

Proof. The proof is given in Appendix A. □

Using Proposition 1, we suggest replacing $\mathfrak{m}_{\mathbf{S}}(\mathbf{C},\mathbf{W})$ with $\widehat{\mathfrak{m}}_{\mathbf{S}}(\mathbf{C},\mathbf{W})$ in the equivalent original Problem (8) to yield:

$$\underset{\mathbf{W}\in\mathcal{W}^{L'},\,\mathbf{C}\in\mathcal{C}^{K'}}{\text{maximize}} \ \frac{1}{L'}\sum_{\ell=1}^{L'}\Re\left(\mathbf{a}_\ell^{\mathsf{H}}\mathbf{w}_\ell\right)+\frac{\omega}{K'}\sum_{k=1}^{K'}\Re\left(\mathbf{b}_k^{\mathsf{H}}\mathbf{c}_k\right) \tag{10}$$

$$\text{s.t.} \ \ (\forall k\in[K'],\forall \ell\in[L']) \ \ \sqrt{\mathbf{c}_k^{\mathsf{H}}\mathbf{G}_{\mathrm{rx}}\mathbf{c}_k}\sqrt{\mathbf{w}_\ell^{\mathsf{H}}\mathbf{G}_{\mathrm{tx}}\mathbf{w}_\ell} \le \varepsilon\,.$$

Problem (10) is a restriction of Problem (7), in the sense that any feasible codebook pair for (10) is also feasible for (7) by Proposition 1. Due to the potential bound gap in (9), however, a solution to (10) is not necessarily a solution to (7).

Nevertheless, (9) can become tight for some practical situations. For the case $M = N$, for instance, tightness is approximated if the max. SI is reached for a certain pair $\mathbf{c} = \mathbf{w}$ under an SI channel containing a predominant symmetric path $\mathbf{S}(t_0) = \mathbf{s}\mathbf{s}^{\mathsf{H}}$, such that $\mathbf{G}_{\mathrm{tx}} \approx \mathbf{G}_{\mathrm{rx}} \approx \mathbf{s}\mathbf{s}^{\mathsf{H}}$. Thus, we expect $\mathfrak{m}_{\mathbf{S}}(\mathbf{C},\mathbf{W}) \approx \widehat{\mathfrak{m}}_{\mathbf{S}}(\mathbf{C},\mathbf{W})$ under spatially sparse symmetric SI channels, which are relevant for monostatic ISAC [6], [16].

Based on Problem (10), we propose designing a codebook pair $(\bar{\mathbf{C}}, \bar{\mathbf{W}})$ columnwise, by solving $L' + K'$ problems in the following form:

$$\underset{\mathbf{z}\in\mathbb{C}^P}{\text{maximize}} \quad \Re(\mathbf{r}^{\mathsf{H}}\mathbf{z}) \tag{11a}$$

$$\text{s.t.} \quad \mathbf{z}^{\mathsf{H}}\mathbf{G}\mathbf{z} \le \epsilon, \tag{11b}$$

$$\mathbf{z} \in \mathcal{Z}\,, \tag{11c}$$

with $P \in \{M, N\}$, $\mathcal{Z} \in \{\mathcal{W}, \mathcal{C}\}$, and the parameters $\mathbf{r} \in \mathcal{Z}$, $\mathbf{G} \in \mathbb{S}_+^P$, and $\epsilon > 0$ chosen ($\forall \ell \in [L']$, $\forall k \in [K']$) as

$$\begin{aligned}\mathbf{r} = \mathbf{a}_\ell\,,\ \mathbf{G} = \mathbf{G}_{\mathrm{tx}}\,,\ \ \epsilon = \varepsilon\beta,\ \text{for } \bar{\mathbf{w}}_\ell,\\ \mathbf{r} = \mathbf{b}_k\,,\ \mathbf{G} = \mathbf{G}_{\mathrm{rx}}\,,\ \epsilon = \varepsilon\beta^{-1},\ \text{for } \bar{\mathbf{c}}_k,\end{aligned} \tag{12}$$

for $\varepsilon > 0$ in (10) and $\beta > 0$, such that

$$\widehat{\mathfrak{m}}_{\mathbf{S}}(\bar{\mathbf{C}},\bar{\mathbf{W}}) = \Big(\max_{k\in[K']}\underbrace{\bar{\mathbf{c}}_k^{\mathsf{H}}\mathbf{G}_{\mathrm{rx}}\bar{\mathbf{c}}_k}_{\le\varepsilon\beta^{-1}}\max_{\ell\in[L']}\underbrace{\bar{\mathbf{w}}_\ell^{\mathsf{H}}\mathbf{G}_{\mathrm{tx}}\bar{\mathbf{w}}_\ell}_{\le\varepsilon\beta}\Big)^{1/2} \le \varepsilon\,.$$

Denoting the optimal value of (11) with $f_{\mathcal{Z}}(\mathbf{r},\mathbf{G},\epsilon)$, we can express the codebook deviations attained through this scheme as $\sigma_{\mathrm{tx}}^2 = 1 - \frac{1}{L'}\sum_{\ell=1}^{L'} f_{\mathcal{W}}(\mathbf{a}_\ell, \mathbf{G}_{\mathrm{tx}}, \varepsilon\beta)$ and $\sigma_{\mathrm{rx}}^2 = 1 - \frac{1}{K'}\sum_{k=1}^{K'} f_{\mathcal{C}}(\mathbf{b}_k, \mathbf{G}_{\mathrm{rx}}, \varepsilon\beta^{-1})$. Optimization theory can prove that $f_{\mathcal{Z}}(\mathbf{r},\mathbf{G},\epsilon)$ is a monotonically increasing function of ϵ [35], and thus σ_{tx}^2 and σ_{rx}^2 are monotonically decreasing on ε for $\beta > 0$.

The possibility to trade off TX and RX codebook deviation, embodied by ω in (7), is provided instead by β in (11)–(12). In symmetric scenarios where $\mathbf{A} = \mathbf{B}$ and $\mathbf{G}_{\mathrm{tx}} = \mathbf{G}_{\mathrm{rx}}$, we expect the balance point $\beta = 1$ to yield a good sensing SNR for given ε, based on the observation that the RX echo power for a target at an angular direction θ is proportional to the product $f_{\mathcal{C}}(\mathbf{b}_{k_\theta}, \mathbf{G}_{\mathrm{rx}}, \varepsilon\beta^{-1}) f_{\mathcal{W}}(\mathbf{a}_{\ell_\theta}, \mathbf{G}_{\mathrm{tx}}, \varepsilon\beta)$ for certain $k_\theta = \ell_\theta \in [L']$. The value of β can be alternatively determined with respect to antenna saturation, while ε can be set in relation to the quantization noise. The choice of ε and β with respect to said criteria is analyzed in detail in Section IV.

We refer to the solutions to (11)–(12) as *codebooks with integral split for self-interference reduction (CISSIR)*. In the following Sections III-B–III-C, we particularize Problem (11)

Algorithm 1 Tapered CISSIR optimization.

Require: $\mathbf{S}(t), \mathbf{A}, \mathbf{B}, \varepsilon, \beta$
$\mathbf{G}_{\mathrm{tx}}, \mathbf{G}_{\mathrm{rx}} \leftarrow$ IntegralSplit($\mathbf{S}(t)$) ▷ Def. 1
$\mathbf{W} \leftarrow$ SpectralCodebook($\mathbf{A}, \mathbf{G}_{\mathrm{tx}}, \varepsilon\beta$)
$\mathbf{C} \leftarrow$ SpectralCodebook($\mathbf{B}, \mathbf{G}_{\mathrm{rx}}, \varepsilon\beta^{-1}$)
return $\mathbf{W}$, $\mathbf{C}$
function SpectralCodebook($\mathbf{R}, \mathbf{G}, \epsilon$)
  $\mathbf{Q}, \mathbf{\Gamma} \leftarrow$ SpectralDecomposition($\mathbf{G}$) ▷ Prop. 2
  for $i = 1, 2, \ldots, J :=$NumColumns($\mathbf{G}$) **do**
    $\mathbf{r} \leftarrow [\mathbf{R}]_{:,i}$
    if $\epsilon < \mathbf{r}^{\mathsf{H}}\mathbf{G}\mathbf{r}$ **then**
      $\mathbf{z}_i \leftarrow$ OptimizeVector($\mathbf{r}, \epsilon, \mathbf{Q}, \mathbf{\Gamma}$)
    else
      $\mathbf{z}_i \leftarrow \mathbf{r}$
    end if
  end for
  return $[\mathbf{z}_1, \mathbf{z}_2, \ldots, \mathbf{z}_J]$
end function
function OptimizeVector($\mathbf{r}, \epsilon, \mathbf{Q}, \mathbf{\Gamma}$)
  $\mathcal{P}(\nu) \leftarrow$ BuildPoly($\mathbf{r}, \epsilon, \mathbf{Q}, \mathbf{\Gamma}$) ▷ Prop. 2
  $\nu_\star \leftarrow$ LargestRealRoot($\mathcal{P}(\nu)$)
  $\check{\mathbf{z}} \leftarrow \mathbf{Q}(\mathbf{\Gamma} + \nu_\star\mathbf{I})^{-1}\mathbf{Q}^{\mathsf{H}}\mathbf{r}$
  return $\check{\mathbf{z}}/\|\check{\mathbf{z}}\|_2$
end function

for specific choices of $\mathcal{C}$ and $\mathcal{W}$, but we first remark some general properties induced by the unit power constraint (1) from the system model in Section II-A.

Remark 1. Problem (11) is still nonconvex for $\mathcal{Z} \in \{\mathcal{W}_\triangleright, \mathcal{W}_\oslash, \mathcal{C}_\triangleright, \mathcal{C}_\oslash\}$ due to (1). A straightforward convex relaxation can be obtained by replacing $\mathcal{Z}$ with its convex hull.

Remark 2. The optimal value fulfills $f_{\mathcal{Z}}(\mathbf{r}, \mathbf{G}, \epsilon) \leq 1$, and the equality is attained with $\mathbf{z}_\star = \mathbf{r}$ if $\epsilon \geq \mathbf{r}^{\mathsf{H}}\mathbf{G}\mathbf{r}$. To see this, we note that:

$$(\forall \mathbf{z}_\star \in \mathcal{Z}) \quad \Re(\mathbf{r}^{\mathsf{H}}\mathbf{z}_\star) \leq \left|\mathbf{r}^{\mathsf{H}}\mathbf{z}_\star\right| \leq \|\mathbf{r}\|_2 \, \|\mathbf{z}_\star\|_2 = 1\,,$$

where the equality follows from (1). The inequalities above become tight for $\mathbf{z}_\star = \mathbf{r}$, but $\mathbf{r}$ is only feasible if $\epsilon \geq \mathbf{r}^{\mathsf{H}}\mathbf{G}\mathbf{r}$.

B. Tapered beamforming

We first particularize Problem (11) to tapered beamforming, where amplitude and phase can be controlled continuously and individually for every antenna element. As we will see, this case admits a semi-closed form solution that relies only on matrix decompositions and other linear algebra operations.

For tapering, we have $\mathcal{W} = \mathcal{W}_\triangleright$ and $\mathcal{C} = \mathcal{C}_\triangleright$, and Problem (11) takes the form:

$$\begin{aligned} \underset{\mathbf{z}\in\mathbb{C}^P}{\text{maximize}} \quad & \Re(\mathbf{r}^{\mathsf{H}}\mathbf{z}) && \text{(13a)} \\ \text{s.t.} \quad & \mathbf{z}^{\mathsf{H}}\mathbf{G}\mathbf{z} \leq \epsilon, && \text{(13b)} \\ & \mathbf{z}^{\mathsf{H}}\mathbf{z} = 1\,. && \text{(13c)} \end{aligned}$$

Although Problem (13) is nonconvex, it can be solved efficiently as stated below and outlined in Algorithm 1.

Algorithm 2 Phased CISSIR optimization.

Require: $\mathbf{S}(t), \mathbf{A}, \mathbf{B}, \varepsilon, \beta$
$\mathbf{G}_{\mathrm{tx}}, \mathbf{G}_{\mathrm{rx}} \leftarrow$ IntegralSplit($\mathbf{S}(t)$) ▷ Def. 1
$\mathbf{W} \leftarrow$ SdpCodebook($\mathbf{A}, \mathbf{G}_{\mathrm{tx}}, \varepsilon\beta$)
$\mathbf{C} \leftarrow$ SdpCodebook($\mathbf{B}, \mathbf{G}_{\mathrm{rx}}, \varepsilon\beta^{-1}$)
return $\mathbf{W}$, $\mathbf{C}$
function SdpCodebook($\mathbf{R}, \mathbf{G}, \epsilon$)
  for $i = 1, 2, \ldots, J :=$NumColumns($\mathbf{G}$) **do**
    $\mathbf{r} \leftarrow [\mathbf{R}]_{:,i}$
    $\tilde{\mathbf{Z}} \leftarrow$ SolveSdp($\mathbf{r}, \mathbf{G}, \epsilon$) ▷ (15a)–(15d)
    $\tilde{\mathbf{z}} \leftarrow \sqrt{\sigma_{\max}(\tilde{\mathbf{Z}})}\mathbf{v}_{\max}(\tilde{\mathbf{Z}})$
    $\mathbf{z}_i \leftarrow \tilde{\mathbf{z}}(\tilde{\mathbf{z}}^{\mathsf{H}}\mathbf{r}/\left|\tilde{\mathbf{z}}^{\mathsf{H}}\mathbf{r}\right|)$
  end for
  return $[\mathbf{z}_1, \mathbf{z}_2, \ldots, \mathbf{z}_J]$
end function

Proposition 2. *Consider a spectral decomposition* $\mathbf{G} = \mathbf{Q}\mathbf{\Gamma}\mathbf{Q}^{\mathsf{H}} \neq \mathbf{0}$ *of the matrix* $\mathbf{G} \in \mathbb{S}_+^P$ *in* (13b)*, where* $\mathbf{Q}$ *is unitary and* $\mathbf{\Gamma}$ *a diagonal matrix with diagonal entries given by* $(\forall p \in [P])\ \sigma_p := [\mathbf{\Gamma}]_{p,p}$*. Problem (13) admits a solution*

$$\mathbf{z}_\star = \check{\mathbf{z}}/\left\|\check{\mathbf{z}}\right\|_2\,, \quad \text{with} \quad \check{\mathbf{z}} := \mathbf{Q}\left(\mathbf{\Gamma} + \nu_\star\mathbf{I}\right)^{-1}\mathbf{Q}^{\mathsf{H}}\mathbf{r}\,,$$

where $\nu_\star$ *is a positive root of the real polynomial*

$$\mathcal{P}(\nu) := \sum_{p=1}^{P} (\sigma_p - \epsilon)\left|\mathbf{q}_p^{\mathsf{H}}\mathbf{r}\right|^2 \prod_{q\neq p} (\sigma_q + \nu)^2\,,$$

under certain sufficient conditions depending on the rank of $\mathbf{G}$*. In particular,* $\mathbf{z}_\star$ *exists if either:*

i) $\operatorname{rank}(\mathbf{G}) < P$ *and* $\epsilon \in (0, \mathbf{r}^{\mathsf{H}}\mathbf{G}\mathbf{r})$*, or*
ii) $\operatorname{rank}(\mathbf{G}) = P$ *and* $\epsilon \in (\bar{\sigma}(\mathbf{r}, \mathbf{G}), \mathbf{r}^{\mathsf{H}}\mathbf{G}\mathbf{r})$*, with*

$$\bar{\sigma}(\mathbf{r}, \mathbf{G}) := \frac{\sum_{p=1}^{P}\left|\mathbf{q}_p^{\mathsf{H}}\mathbf{r}\right|^2/\sigma_p}{\sum_{p=1}^{P}\left|\mathbf{q}_p^{\mathsf{H}}\mathbf{r}\right|^2/\sigma_p^2}\,.$$

Proof. The proof is given in Appendix B. □

C. Phased-array optimization

In contrast to the previous section, the phased-array case does not admit a direct solution. Nevertheless, we will show that phased-array codebooks can be obtained via semidefinite programming (SDP) [30], as described in Algorithm 2.

Phased array codebooks $\mathcal{C}_\oslash$ and $\mathcal{W}_\oslash$ yield the following form of Problem (11):

$$\begin{aligned} \underset{\mathbf{z}\in\mathbb{C}^P}{\text{maximize}} \quad & \Re(\mathbf{r}^{\mathsf{H}}\mathbf{z}) \\ \text{s.t.} \quad & \mathbf{z}^{\mathsf{H}}\mathbf{G}\mathbf{z} \leq \epsilon, \\ (\forall p \in [P]) \quad & \mathbf{z}^{\mathsf{H}}\mathbf{e}_p\mathbf{e}_p^{\mathsf{T}}\mathbf{z} = 1/P\,, \end{aligned} \tag{14}$$

where $\mathbf{e}_p = [\mathbf{I}]_{:,p}$ is the p-th standard basis vector. We will now propose a method to solve (14) via SDP.

Proposition 3. *A solution to Problem (14) is given by*

$$\mathbf{z}_\star = \tilde{\mathbf{z}}\frac{\tilde{\mathbf{z}}^{\mathsf{H}}\mathbf{r}}{|\tilde{\mathbf{z}}^{\mathsf{H}}\mathbf{r}|}, \quad \tilde{\mathbf{z}} = \sqrt{\sigma_{\max}(\tilde{\mathbf{Z}})}\mathbf{v}_{\max}(\tilde{\mathbf{Z}})\,,$$

where $\sigma_{\max}(\tilde{\mathbf{Z}})$ and $\mathbf{v}_{\max}(\tilde{\mathbf{Z}})$ are the largest eigenvalue and the corresponding eigenvector, respectively, of a solution $\tilde{\mathbf{Z}}$ to the following nonconvex SDP problem:

$$\begin{aligned} \underset{\mathbf{Z}\in\mathbb{S}^P}{\text{maximize}} \quad & \langle \mathbf{r}\mathbf{r}^{\mathsf{H}}, \mathbf{Z}\rangle && \text{(15a)}\\ \text{s.t.} \quad & \langle \mathbf{G}, \mathbf{Z}\rangle \leq \epsilon, && \text{(15b)}\\ (\forall p \in [P]) \quad & \langle \mathbf{e}_p\mathbf{e}_p^{\mathsf{H}}, \mathbf{Z}\rangle = 1/P\,, && \text{(15c)}\\ & \mathbf{Z} \succcurlyeq \mathbf{0}\,, && \text{(15d)}\\ & \operatorname{rank}(\mathbf{Z}) \leq 1\,. && \text{(15e)} \end{aligned}$$

Proof. We first note that any solution $\mathbf{z}_\star$ to (14) must fulfill $\Re(\mathbf{r}^{\mathsf{H}}\mathbf{z}_\star) = \left|\mathbf{r}^{\mathsf{H}}\mathbf{z}_\star\right|$. This follows from the fact that, for any feasible $\mathbf{z}_{\mathrm{f}}$, we can construct another feasible $\tilde{\mathbf{z}}_{\mathrm{f}}$ such that

$$\Re(\mathbf{r}^{\mathsf{H}}\mathbf{z}_{\mathrm{f}}) \leq \left|\mathbf{r}^{\mathsf{H}}\mathbf{z}_{\mathrm{f}}\right| = \Re(\mathbf{r}^{\mathsf{H}}\tilde{\mathbf{z}}_{\mathrm{f}})\,, \quad \tilde{\mathbf{z}}_{\mathrm{f}} = \mathbf{z}_{\mathrm{f}}\left(\mathbf{z}_{\mathrm{f}}^{\mathsf{H}}\mathbf{r}/\left|\mathbf{z}_{\mathrm{f}}^{\mathsf{H}}\mathbf{r}\right|\right).$$

Consequently, we can substitute the objective function in (14) with $\left|\mathbf{r}^{\mathsf{H}}\mathbf{z}\right|^2 = \mathbf{z}^{\mathsf{H}}\mathbf{r}\mathbf{r}^{\mathsf{H}}\mathbf{z}$. In addition to this, we note the trace circular property ($\forall \mathbf{M} \in \mathbb{S}^M$, $\forall \mathbf{z} \in \mathbb{C}^M$):

$$\mathbf{z}^{\mathsf{H}}\mathbf{M}\mathbf{z} = \operatorname{tr}(\mathbf{z}^{\mathsf{H}}\mathbf{M}\mathbf{z}) = \operatorname{tr}(\mathbf{z}\mathbf{z}^{\mathsf{H}}\mathbf{M}) = \langle \mathbf{M}, \mathbf{z}\mathbf{z}^{\mathsf{H}}\rangle\,,$$

which allows us to express Problem (14) in terms of inner products as (15), such that $\tilde{\mathbf{Z}} = \mathbf{z}_\star\mathbf{z}_\star^{\mathsf{H}}$ and $\mathbf{z}_\star$ solves (14). □

A convex relaxation of Problem (15) can be obtained by dropping the nonconvex constraint (15e). A solution $\tilde{\mathbf{Z}}$ to the convex SDP problem (15a)–(15d) is not guaranteed to have rank one, but we can further elaborate on $\operatorname{rank}(\tilde{\mathbf{Z}})$ by relaxing constraint (15c):

$$\begin{aligned} \underset{\mathbf{Z}\in\mathbb{S}^P}{\text{maximize}} \quad & \langle \mathbf{r}\mathbf{r}^{\mathsf{H}}, \mathbf{Z}\rangle \\ \text{s.t.} \quad & \langle \mathbf{G}, \mathbf{Z}\rangle \leq \epsilon, \\ (\forall p \in [P]) \quad & \langle \mathbf{e}_p\mathbf{e}_p^{\mathsf{H}}, \mathbf{Z}\rangle \leq 1/P\,, \\ & \mathbf{Z} \succcurlyeq \mathbf{0}\,. \end{aligned} \tag{16}$$

Problem (16) is also known as a *semidefinite packaging* problem, and Sagnol [36] proved that it always has a rank-one solution. Therefore, the solution $\tilde{\mathbf{Z}}$ to (15a)–(15d) will also have rank one if it coincides with a solution to (16) for given $\mathbf{r}$, $\mathbf{G}$, and ϵ.

Furthermore, we know that $\exists\, \epsilon_\star \leq \mathbf{r}^{\mathsf{H}}\mathbf{G}\mathbf{r}$ such that $\forall \epsilon \geq \epsilon_\star$ $\operatorname{rank}(\tilde{\mathbf{Z}}) = 1$ (cf. Remark 2). Unfortunately, $\epsilon_\star$ cannot be easily narrowed down further, but we can still assess the rank of $\tilde{\mathbf{Z}}$ through the ratio between its spectral and nuclear norms:

$$\Upsilon(\tilde{\mathbf{Z}}) \coloneqq \frac{\|\tilde{\mathbf{Z}}\|_2}{\|\tilde{\mathbf{Z}}\|_*} = \frac{\sigma_{\max}(\tilde{\mathbf{Z}})}{\operatorname{tr}(\tilde{\mathbf{Z}})} \in [1/P\,,\ 1]\,, \tag{17}$$

for which we know that $\Upsilon(\tilde{\mathbf{Z}}) = 1 \iff \operatorname{rank}(\tilde{\mathbf{Z}}) = 1$. In Section V, we use this fact to evaluate the feasibility of Algorithm 2 in our scenarios.

IV. Performance bounds and parameter selection

The proposed Algorithms 1–2 in Section III aim to reduce the max. SI $\mathfrak{m}_{\mathbf{S}}(\mathbf{C}, \mathbf{W})$ in (5) according to the parameters ε and β. We analyze now the effect of SI before the ADCs for the hybrid-beamforming system in Section II-A, in order to provide recommendations for the choice of said parameters.

In Section IV-A, we derive a theoretical bound on the variance of the quantization noise introduced by the ADC, while we also take into account other dynamic-range limitations and saturation. In Section IV-B, we extend the derived bound to the SNR for analog orthogonal frequency-division multiplexing (OFDM) radar, a popular ISAC setup [1]–[7]. Finally, in Section IV-C we discuss how to select the target SI ε based on the derived bounds and our signal knowledge.

A. Self-interference impact at the analog-to-digital converter

ADCs have limited dynamic range, which can be critical for ISAC in the face of SI. In particular, the ADC bit resolution Q causes signal quantization, modeled as $u_k[i]$ in (4) by following the well-established assumption of uniform white quantization noise [37]. That is, we assume $u_k[i]$ is independent of the ADC's input signal, with i.i.d. $\Re(u_k[i])$ and $\Im(u_k[i])$ drawn from $\mathcal{U}(-\frac{\Delta}{2}, \frac{\Delta}{2})$. The quantization step Δ can then be expressed in terms of the ADC's full-scale value y_{fs} and the bit resolution Q as $\Delta = 2y_{\mathrm{fs}}/2^Q$, for which the quantization noise power equals

$$\sigma_{\mathrm{Q}}^2 \coloneqq \mathbb{E}[|u_k[i]|^2] = 2\frac{\Delta^2}{12} = \frac{2y_{\mathrm{fs}}^2}{3}2^{-2Q} = \mathfrak{b}_{\mathrm{Q}}y_{\mathrm{fs}}^2. \tag{18}$$

We write $\mathfrak{b}_{\mathrm{Q}}$ in (18) to stress the relation $\sigma_{\mathrm{Q}}^2 \propto y_{\mathrm{fs}}^2$, as well as to extend our analysis to other sources of dynamic-range limitations, such as logarithmic ADCs or finite-precision arithmetic. With this in mind, we can minimize σ_{Q}^2 via gain control by setting y_{fs} to the smallest possible value above saturation. Under our TDD assumption, we can leverage the absence of uplink signals and the full knowledge of both the transmitted $\mathbf{x}(t)$ and the calibrated SI channel $\mathbf{S}(t)$ to select

$$y_{\mathrm{fs}} = \gamma \max_{\substack{t\in[0,T+T_{\mathrm{c}}]\\ k\in[K]}} \left|\sum_{\ell=1}^{L}\left(\left(\mathbf{c}_{\imath(k)}^{\mathsf{H}}\mathbf{S}\,\mathbf{w}_{\jmath(\ell)}\right) * x_\ell\right)(t)\right|, \tag{19}$$

where we choose a back-off term $\gamma > 1$ to account for the unknown radar channel $\mathbf{H}_{\mathrm{r}}(t)$. The condition to avoid saturation is

$$\gamma \geq \frac{\max_{t,k}\left|\sum_{\ell=1}^{L}\left(\left(\mathbf{c}_{\imath(k)}^{\mathsf{H}}\left(\mathbf{H}_{\mathrm{r}}+\mathbf{S}\right)\mathbf{w}_{\jmath(\ell)}\right) * x_\ell\right)(t)\right|}{\max_{t,k}\left|\sum_{\ell=1}^{L}\left(\left(\mathbf{c}_{\imath(k)}^{\mathsf{H}}\mathbf{S}\,\mathbf{w}_{\jmath(\ell)}\right) * x_\ell\right)(t)\right|}\,.$$

Therefore, we can set γ fairly close to 1 in practice, since the contribution from the SI channel $\mathbf{S}(t)$ is typically orders of magnitude larger than the backscattered power over $\mathbf{H}_{\mathrm{r}}(t)$.

We will now show how the sampling scheme in (18)–(19) yields an upper bound on the ADC noise as a function of the max. SI. The derived bound only depends on generic TX-signal properties, namely the TX power P_{tx} and the peak-to-average power ratio (PAPR) of each signal, ($\forall \ell \in [L]$) ρ_{x_ℓ}:

$$P_{\mathrm{tx}} \coloneqq \sum_{\ell=1}^{L}\frac{1}{T}\int_0^T |x_\ell(t)|^2\, dt = \frac{1}{T}\sum_{\ell=1}^{L}|x_\ell|_2^2\,, \tag{20}$$

$$\rho_{x_\ell} \coloneqq T|x_\ell|_\infty^2/|x_\ell|_2^2\,. \tag{21}$$

Lemma 1. *Consider the system model in Section II, with the max. SI $\mathfrak{m}_{\mathbf{S}}(\mathbf{C}, \mathbf{W})$ in* (5)*, the RX signal $\mathbf{y}(t)$ in* (3)*, sampled at $1/T_{\mathrm{S}}$ to obtain $\hat{\mathbf{y}}[i]$ in* (4)*. Assuming quantization noise, RX*

gain control as per (18)–(19)*, and the TX-signal properties in* (20)–(21)*, then we have:*

$$\mathbb{E}\left[\|\hat{\mathbf{y}}[i]-\mathbf{y}(iT_{\mathrm{S}})\|_2^2\right]=\sum_{k=1}^{K}\left(\sigma_{\mathrm{T}}^2+\sigma_{\mathrm{Q}}^2\right)\leq$$

$$K\sigma_{\mathrm{T}}^2+KP_{\mathrm{tx}}\gamma^2\mathfrak{b}_{\mathrm{Q}}\mathfrak{m}_{\mathbf{S}}^2(\mathbf{C},\mathbf{W})\sum_{\ell=1}^{L}\rho_{x_\ell}. \tag{22}$$

Proof. The proof is given in Appendix C. □

Corollary 1. *Let us assume the same system model as for Lemma 1, but with the channel propagation represented by discrete convolution with* $\bar{\mathbf{H}}[i]=\bar{\mathbf{H}}_{\mathrm{r}}[i]+\bar{\mathbf{S}}[i]$*, i.e., (*$\forall k\in[K]$*):*

$$\bar{y}_k[i]=\sum_{\ell=1}^{L}\left(\left(\mathbf{c}_k\bar{\mathbf{H}}\mathbf{w}_\ell\right)*\bar{x}_\ell\right)[i],\quad(\forall\ell\in[L])\ \bar{x}_\ell[i]\coloneqq x_\ell(iT_{\mathrm{S}})\,.$$

Then, (22) *still holds with* $J=\lfloor(T+T_{\mathrm{c}})/T_{\mathrm{S}}\rfloor$ *and* $\mathfrak{m}_{\bar{\mathbf{S}}}(\mathbf{C},\mathbf{W})=\max_{k,\ell}\sum_{i=1}^{J}\left|\mathbf{c}_k\bar{\mathbf{S}}[i]\mathbf{w}_\ell\right|$.

Proof. The proof follows from the fact that Young's inequality in Lemma 1's proof also applies to the discrete convolution [38, Theorem (20.18)]. □

Lemma 1 allows us to assess the quantization noise induced by multipath SI for given beamforming codebooks, which we validate in Section V via simulations, thanks to Corollary 1. These results also provide us with a rule to select the target SI ε in Problems (7) and (11), as we discuss in Section IV-C.

As for β in (12), while $\beta=1$ is a sensible choice (cf. Section III-A), other values of β may be preferred if the system is susceptible to RX antenna saturation. In this sense, we provide the following Proposition 4 as a rule to choose β for given ε so that ($\forall m\in[M]$) the peak power at the m-th RX antenna remains below a certain P_{sat}, i.e.:

$$|\mathring{y}_m|_\infty^2\leq P_{\mathrm{sat}}\,,\quad\mathring{y}_m(t)\coloneqq\sum_{\ell=1}^{L}\left(\left(\mathbf{e}_m^{\mathsf{T}}\mathbf{H}\,\mathbf{w}_{\jmath(\ell)}\right)*x_\ell\right)(t)\,. \tag{23}$$

Proposition 4. *Assume the system model from Lemma 1 and the optimization scheme given by* (11)–(12)*. Then, the condition* (23) *is satisfied if*

$$\varepsilon\beta=\frac{P_{\mathrm{sat}}}{\gamma^2P_{\mathrm{tx}}\sum_{\ell\in[L']}\rho_{x_\ell}\max_{m\in[M]}[\mathbf{G}_{\mathrm{rx}}]_{m,m}}\,.$$

Proof. Noting that $\{\mathring{y}_m(t)\}_{m=1}^M$ is a special case of (3) for $K=K'=M$ and $\mathbf{C}=\mathbf{I}\in\mathbb{C}^{M\times M}$, the proof follows from the same arguments as in Lemma 1's proof, and from the application of Proposition 1 to $\mathfrak{m}_{\mathbf{S}}(\mathbf{I},\mathbf{W})$. □

B. Signal-to-noise ratio for analog OFDM radar

Lemma 1 provides a bound on noise variance as a function of the max. SI $\mathfrak{m}_{\mathbf{S}}(\mathbf{C},\mathbf{W})$. Based on this bound, we focus now on analog beamforming and OFDM radar to extend our performance analysis to the sensing SNR, which is the main performance indicator for sensing detection and estimation [9].

Under analog beamforming, we have $K=L=1$ RF chains. As a result, we only transmit a signal $\mathbf{x}(t)=x(t)\in\mathbb{C}$, and we receive $\mathbf{y}(t)=y(t)\in\mathbb{C}$ as:

$$y(t)=((\underbrace{\mathbf{c}_\circ^{\mathsf{H}}\mathbf{S}\mathbf{w}_\circ}_{=:h_{\mathrm{si}}}+\underbrace{\mathbf{c}_\circ^{\mathsf{H}}\mathbf{H}_{\mathrm{r}}\mathbf{w}_\circ}_{=:h_{\mathrm{r}}})*x)(t)=y_{\mathrm{si}}(t)+y_{\mathrm{r}}(t)\,, \tag{24}$$

where $\mathbf{c}_\circ\in\mathbb{C}^M$ and $\mathbf{w}_\circ\in\mathbb{C}^N$ form our selected TX-RX beamforming pair. This beamforming pair yields the single-antenna equivalent channels $h_{\mathrm{si}}(t)$ and $h_{\mathrm{r}}(t)$, which we assume passband filtered according to the signal bandwidth B.

Furthermore, if we employ OFDM waveforms, we can assume our TX signal to be stationary with almost flat power spectral density $X(f)$ [6], [9]. In other words, ($\forall f\in[f_{\mathrm{c}}-B/2,f_{\mathrm{c}}+B/2]$) $X(f)\approx P_{\mathrm{tx}}/B$, and hence:

$$\mathbb{E}[|y_{\mathrm{r}}(t)|^2]=\zeta\frac{P_{\mathrm{tx}}}{B}\,|h_{\mathrm{r}}|_2^2\approx\int_{f_{\mathrm{c}}-B/2}^{f_{\mathrm{c}}+B/2}\frac{P_{\mathrm{tx}}}{B}|H_{\mathrm{r}}(f)|^2\,df\,, \tag{25}$$

with $\zeta\approx1$. Assuming favorable Nyquist conditions so that $\mathbb{E}[|y_{\mathrm{r}}(iT_{\mathrm{S}})\,|^2]=\mathbb{E}[|y_{\mathrm{r}}(t)|^2]$, we can combine (25) with Lemma 1 to bound the SNR of $y_{\mathrm{r}}(t)$ from (4) as:

$$\mathrm{SNR}=\frac{\mathbb{E}[|y_{\mathrm{r}}(t)|^2]}{\sigma_{\mathrm{T}}^2+\sigma_{\mathrm{Q}}^2}\geq\frac{\zeta\,|h_{\mathrm{r}}|_2^2\,P_{\mathrm{tx}}/B}{\sigma_{\mathrm{T}}^2+\gamma^2\mathfrak{b}_{\mathrm{Q}}\mathfrak{m}_{\mathbf{S}}^2(\mathbf{C},\mathbf{W})P_{\mathrm{tx}}\rho_x}\,, \tag{26}$$

which relates to the Cramèr-Rao lower bound (CRLB) for range estimation with a frequency-flat matched filter [9] as

$$\mathrm{CRLB}=\frac{c^2}{4\,\mathrm{SNR}\cdot B_{\mathrm{rms}}^2}=\frac{c^2}{4\,\mathrm{SNR}\cdot B^2\pi^2/3}\,, \tag{27}$$

with c the speed of light. The expression above considers Gaussian noise, which is not true in general for $u_k[i]$. However, we can invoke the central limit theorem if the matched filter is long enough, as it is expected for OFDM radar [5], [6], to assume that the filtered noise is approximately Gaussian. Hence, we may still use (27) in practice to assess sensing performance via (26) with respect to the max. SI $\mathfrak{m}_{\mathbf{S}}(\mathbf{C},\mathbf{W})$ and the target SI ε.

Nevertheless, choosing ε from (26) is challenging in practice, as we often lack the following information:

1) The radar channel $\mathbf{H}_{\mathrm{r}}(t)$, and thus $h_{\mathrm{r}}(t)$. Even if we know $\mathbf{H}_{\mathrm{r}}(t)$, we cannot compute $|h_{\mathrm{r}}|_2$ before optimizing ($\mathbf{c}_\circ$, $\mathbf{w}_\circ$). However, we can approximate it from the reference beamforming pair ($\mathbf{b}_\circ$, $\mathbf{a}_\circ$) as $|h_{\mathrm{r}}|_2\approx\left|\mathbf{b}_\circ^{\mathsf{H}}\mathbf{H}_{\mathrm{r}}\mathbf{a}_\circ\right|_2$, if the codebook deviations σ_{tx}^2 and σ_{rx}^2 in (6) are low enough.
2) The PAPR ρ_x, since the signal $x(t)$ may also be unknown during optimization.

To address this issue, we suggest a more practical approach in Section IV-C.

C. Selection of the target self-interference

To set the target SI ε in Algorithms 1–2, we first suggest fixing a target quantization noise $\sigma_\star^2$, either from (26) if $|h_{\mathrm{r}}|_2^2$ is known, or with respect to the thermal noise σ_{T}^2 otherwise. From Lemma 1, we select the target SI as

$$\varepsilon=\frac{\sigma_\star}{\gamma\sqrt{\mathfrak{b}_{\mathrm{Q}}P_{\mathrm{tx}}\bar{\varrho}_{\mathbf{x}}}}\,, \tag{28}$$

which guarantees $\sigma_{\mathrm{Q}}^2\leq\sigma_\star^2$. The estimated PAPR $\bar{\varrho}_{\mathbf{x}}>0$ is computed from the available information on $\mathbf{x}(t)$ during optimization. Some options to compute $\bar{\varrho}_{\mathbf{x}}$ include:

1) Matched optimization: In the best-case scenario where we do know $\mathbf{x}(t)$, we can just choose $\bar{\varrho}_{\mathbf{x}} = \sum_{\ell=1}^{L} \rho_{x_\ell}$ in (28) and solve (11) only for the vectors given by $\imath$ and $\jmath$. This option may be relevant if the optimization algorithm is fast enough to be run for every new TX symbol, e.g., if it has a semi-closed form as in Section III-B.

2) Average optimization: In certain setups, it might suffice to ensure that the quantization noise variance is below $\sigma_\star^2$ only for the average TX symbol. In this case, the codebooks can be optimized a priori with $\bar{\varrho}_{\mathbf{x}} = \sum_{\ell=1}^{L} \mathbb{E}[\rho_{x_\ell}]$.

3) Quantile optimization: If a certain noise level must be guaranteed, yet memory and speed limitations rule out the previous methods, then we can make $\bar{\varrho}_{\mathbf{x}} = \sum_{\ell=1}^{L} \mathbb{E}[\rho_{x_\ell}]/\alpha$. This PAPR estimate controls the probability of a TX symbol to exceed the noise threshold via Markov's inequality, i.e.:

$$\Pr(\sigma_{\mathrm{Q}}^2 \geq \sigma_\star^2) \leq \alpha\,.$$

V. Numerical results

We corroborate now the presented theoretical analysis of CISSIR with a series of simulation experiments. First, we present some sensing results in Section V-A, which illustrate and validate the performance bounds derived in Section IV. Afterwards, we study the impact of SI reduction on communication, in Section V-B. We continue with an investigation of the communication-sensing trade-off in Section V-C, both for CISSIR and for the baseline LoneSTAR [17]. Finally, we complete our numerical evaluation with a discussion on the time complexity and feasibility of the studied algorithms.

Our simulation environment has been developed from previous work in [40] and is based on Sionna™, a Python library by Nvidia that integrates link-level and ray-tracing simulation tools [31]. Our reference standard is 5G NR FR2. As such, we employ OFDM waveforms in the millimeter wave (mmWave) frequency with quadrature amplitude modulation (QAM), and subcarrier spacing (SCS) according to a given numerology μ [24]. Likewise, our reference beam codebooks $\mathbf{A}$ and $\mathbf{B}$ are given by the columns of a discrete Fourier transform (DFT) matrix with an oversampling factor $O_1 = 4$ [41]. We assume uniform linear arrays (ULAs) with $M = N = 8$ antennas, radiation pattern according to TR 38.901 [39], fixed elevation, and $L' = K' = 27$ beams, corresponding to a full grid over a sector coverage of 120°. Table I contains the complete parameter list.

We simulate the SI channel via ray-tracing, with $D = 2$ paths corresponding to $\mathbf{S}_1(t)$ and $\mathbf{S}_2(t)$ (see Fig. 1). The component $\mathbf{S}_1(t)$ is produced by a spherical wave model, similar to the flat MIMO SI channel in [17]–[19], while we add the clutter $\mathbf{S}_2(t)$ as a wall-reflected path. Leveraging Corollary 1, we approximate the continuous channels by their discrete versions sampled at $T_{\mathrm{S}} \ll 1/B$, and we apply a passband filter to account for the sensing bandwidth B.

We optimize the codebooks via Algorithms 1–2 for tapered beamforming and phased arrays, respectively. We set $\beta = 1$ (and thus $\epsilon = \varepsilon$), which yields the best RX echo power in our setup, as discussed in Section III-A. Unless otherwise noted, we use phased arrays as obtained by Algorithm 2. The convex SDP problem (15a)–(15d) therein is solved with CVXPY and its splitting conic solver [32], which we also use to optimize LoneSTAR.

TABLE I
Simulation parameters

NAME	VALUE		SYMBOL
A. Signal parameters			
Carrier frequency	28	GHz	f_{c}
Wavelength	10.7	mm	λ
Waveform	(cyclic-prefix)	OFDM	
5G NR numerology	3	[24]	μ
Subcarrier spacing	120	kHz	SCS
Symbol duration	9.44	µs	T
Max. channel delay	1.11	µs	T_{c}
B. Antenna parameters			
TX antenna elements	8		N
RX antenna elements	8		M
TX codebook size	27		L'
RX codebook size	27		K'
TX RF chains	1 or 4		L
RX RF chains	1 or 4		K
Ant. element spacing	5.35	mm	$\lambda/2$
Ant. element pattern	TR 38.901	[39]	
Elevation angle	0	°	
Sector coverage	120	°	
C. SI parameters			
Min. TX- RX separation	5.35	mm	$\lambda/2$
Wall distance	4	m	
Wall azimuth	65	°	
Multipath max. SI	-54.5	dB	$\mathfrak{m}_{\mathbf{S}}(\mathbf{B},\mathbf{A})$
Single-path max. SI	-60.6	dB	$\mathfrak{m}_{\mathbf{S}_1}(\mathbf{B},\mathbf{A})$
D. Sensing parameters			
TX power	30	dBm	P_{tx}
Sampling interval	0.51	ns	T_{S}
Number of symbols	1000		
Number of subcarriers	1680		
Bandwidth	200	MHz	B
Modulation	64	QAM	
Target azimuth	-39	°	
Target distance	40	m	
Target radar cross section	1	m^2	
Target RX power	-81.0	dBm	
Thermal noise	-90.8	dBm	σ_{T}^2
ADC bits	6	bit	Q
E. Communication parameters			
UE antennas	1		
Number of subcarriers	420		
Number of symbols	14	(2 pilots)	
Bandwidth	50	MHz	
Modulation	4	QAM	
Code rate	0.7		
Bitrate	62.3	Mbit/s	
Channel model	LoS outdoor UMi	[39]	

A. Sensing performance

Our primary goal, as detailed in Sections II–III, is to design ISAC beam codebooks for which the SI-induced quantization noise at our RX sniffer is reduced. To this aim, we have derived the performance bound (26) for the sensing SNR in Section IV, which we compare now with experimental results.

For this, we simulate a backscatter channel $\mathbf{H}(t) = \mathbf{S}(t) + \mathbf{H}_{\mathrm{r}}(t)$ in a single-target scenario, and we apply the channel to an OFDM signal $x(t)$ (cf. Table I.D) to obtain both $y(t)$, as per (24), and its noisy version $\hat{y}(t)$, according to the quantization scheme in Section IV-A. From $\hat{y}(t)$, we compute a range profile via matched filtering with $x(t)$, as we display in Fig. 2 for two distinct beam pairs pointing towards the target. More specifically, one range profile is obtained for a reference beam

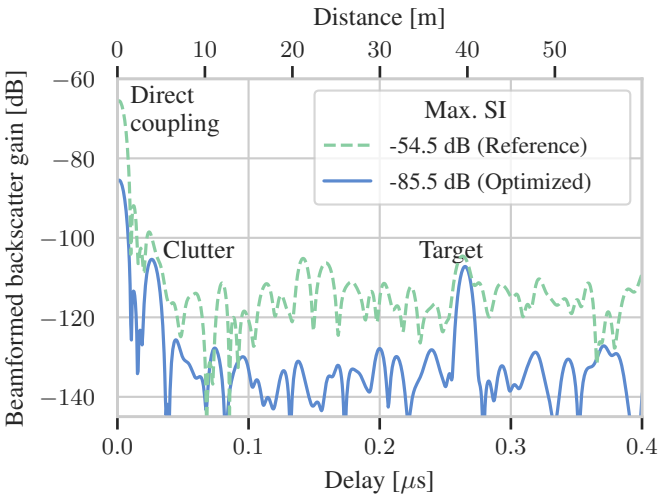


Fig. 2. OFDM range profiles with reference and SI-optimized TX/RX analog beamformers pointing towards a target at −39°.

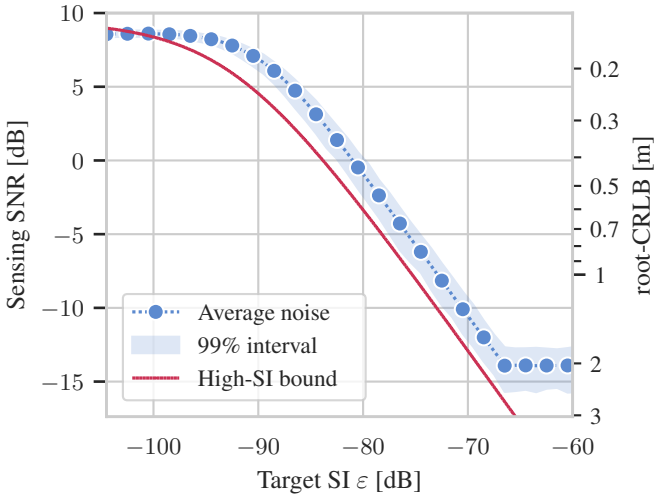


Fig. 3. Simulated sensing SNR and CRLB (symbol-averaged noise and 99 % interval), with approximate bound for high SI, in function of the target SI ε.

pair ($\mathbf{b}_\circ$, $\mathbf{a}_\circ$) under a max. SI around −55 dB, such that the target reflection lies just below the system's dynamic range. In contrast to this, we estimate a second range profile with optimized beams ($\mathbf{c}_\circ$, $\mathbf{w}_\circ$) for a target SI ε near −85 dB, where we observe that the reduced noise floor reveals the target.

This observation encourages us to compare the theoretical SNR bound (26) with the simulated SNR from $\hat{y}(t)$ and the associated square-root CRLB, for different values of ε. The comparison is shown in Fig. 3, where we replace the max. SI $\mathrm{m}_\mathbf{S}(\mathbf{C},\mathbf{W})$ in (26) with ε, we set $|h_\mathrm{r}|_2 = |\mathbf{b}_\circ \mathbf{H}_\mathrm{r} \mathbf{a}_\circ|_2$, we compute the PAPR $\rho_s \approx 9.6$ dB as the average over symbols (cf. Section IV-C2), and we make $\gamma = 1$ and $\zeta \approx 0.98$. We remind the reader that this bound is an a priori approximation of (26) that is only valid for the average noise over TX symbols, and for high SI such that $|h_\mathrm{r}|_2 = \left|\mathbf{c}_\circ^\mathsf{H} \mathbf{H}_\mathrm{r} \mathbf{w}_\circ\right|_2 \approx \left|\mathbf{b}_\circ^\mathsf{H} \mathbf{H}_\mathrm{r} \mathbf{a}_\circ\right|_2$.

In Fig. 3, the SI constraint (11b) only becomes active for ($\mathbf{c}_\circ, \mathbf{w}_\circ$) when the target SI ε is below −68 dB. In that regime, we observe a gap of at most 2.5 dB between the sensing SNR, when the noise is symbol-averaged, and the bound in (26). This bound gap, which arises from Young's inequality (cf. Appendix C), compensates to some extent the SNR fluctuation caused by the PAPR variance over symbols. As expected, this theoretical bound becomes invalid for very low SI, due to a gain loss induced by high codebook deviations $\sigma^2_\mathrm{tx} = \|\mathbf{W} - \mathbf{A}\|^2_\mathrm{F} \,/\, \|\mathbf{A}\|^2_\mathrm{F}$ and $\sigma^2_\mathrm{rx} = \|\mathbf{C} - \mathbf{B}\|^2_\mathrm{F} \,/\, \|\mathbf{B}\|^2_\mathrm{F}$.

To illustrate codebook deviation, we compare some reference TX orthogonal beams from $\mathbf{A}$ with those from $\mathbf{W}$ in Fig. 4. Here, we have chosen very low ε, which leads to higher secondary lobes and gain loss in the main lobe, in the best case. In the worst case, beam misalignment occurs, as can be seen near the sector edges at ±45°. As a result, the angular coverage of CISSIR may become as low as 90°, in contrast to the reference 120° coverage, as we decrease the max. SI.

Motivated by this phenomenon, we investigate next the effect of SI reduction and codebook deviation on communication.

B. Communication performance

We evaluate communication performance via link-level simulations from a base station (BS) towards single-antenna user equipments (UEs), placed randomly on an urban microcell (UMi) sector under line-of-sight (LoS) outdoor conditions [39] and 2 beamforming scenarios. In particular, we either assume a single user served with analog beamforming ($L = 1$), or hybrid multiuser MIMO (MU-MIMO) for 2 users and $L = 4$ beams. The BS selects the L strongest orthogonal beams from the TX codebook, according to [25, Algorithm 1], and feeds them with the zero-forcing (ZF) precoded data streams. In turn, the UEs perform least-squares (LS) channel estimation from 2 OFDM pilot symbols, and linear-minimum-mean-square-error (LMMSE) equalization before decoding. The data in the remaining 12 TX symbols is low-density parity-check (LDPC)-encoded and constitutes a single block (see Table I.E

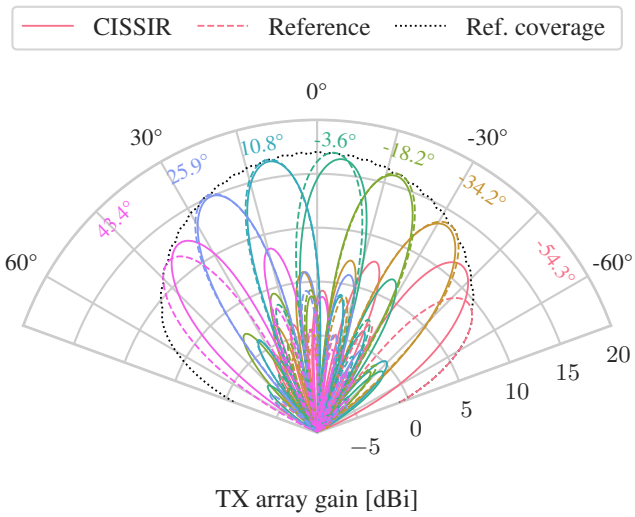


Fig. 4. Orthogonal beams from the TX reference $\mathbf{A}$ (ε =−54.5 dB) and from CISSIR $\mathbf{W}$ (ε =−100.5 dB), with color-matched nominal beam direction.

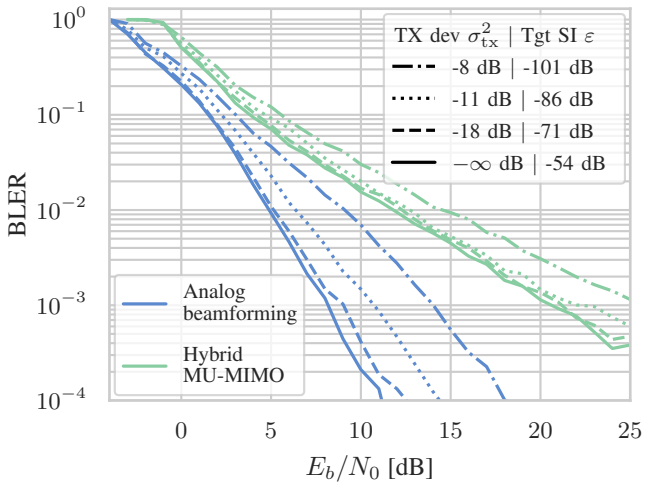


Fig. 5. BLER for different analog and hybrid CISSIR codebooks. The solid lines correspond to the TX reference codebook.

for more details).

We simulate the block error rate (BLER) as a function of the energy per bit to noise power spectral density (E_b/N_0) for the 5G-NR TX reference codebook, as well as for three CISSIR TX codebooks with different levels of target SI ε and codebook deviation σ^2_{tx}. The resulting BLER curves in Fig. 5 show a progressive degradation of the communication performance as we reduce ε, and conversely increase σ^2_{tx} (cf. Section III-A). In the analog scenario, this degradation seems to have a small impact on communication for small values of σ^2_{tx}, which allows us to add 16 dB of extra SI attenuation while losing at most 1 dB of TX power for communication. For the optimized range profile in Fig. 2, on the other hand, the analog BLER curve in Fig. 5 lies within 3 dB apart from the reference codebook. As we further decrease the target SI ε, however, this distance from the reference becomes as large as 6 dB, as a result of the greater codebook deviation.

We can also observe communication degradation for the MU-MIMO results in Fig. 5 as the TX deviation increases. This deterioration is, nevertheless, negligible for σ^2_{tx} below -11 dB, and the performance gap for $\sigma^2_{\text{tx}} \approx -8$ dB is smaller than in the analog case. Hybrid MU-MIMO appears thus to be less sensitive to the chosen beam codebook, which might be caused by the inherent constraints of hybrid beamforming, such as rank-reduced precoding [25].

From these experiments, we conclude that extreme SI reduction may degrade conventional communication, as σ^2_{tx} increases and gives rise to beam misalignment and poorer angular coverage. That being said, communication degradation seems to unfold gently as the target SI is reduced, hinting at a benign operating point where sensing-enhanced, yet communication-transparent codebooks can be realized.

C. Trade-off between self-interference and codebook deviation

From the analysis in Sections V-A–V-B, we consider max. SI and codebook deviations good indicators for sensing and communication performance, respectively. Thus, we use them now to study the sensing-communication trade-off of CISSIR and compare it to that of our baseline LoneSTAR [17].

LoneSTAR codebook optimization, described in [17, Algorithm 1], assumes a frequency-flat MIMO SI channel that can be modeled as a single matrix $\bar{\mathbf{H}} \in \mathbb{C}^{M\times N}$. Given $\bar{\mathbf{H}}$, it minimizes the following SI quantity:

$$\left\|\mathbf{C}\bar{\mathbf{H}}\mathbf{W}\right\|_{\text{F}}^2 = \sum_{k=1}^{K'}\sum_{\ell=1}^{L'} \left|\mathbf{c}_k\bar{\mathbf{H}}\mathbf{w}_\ell\right|^2 , \tag{29}$$

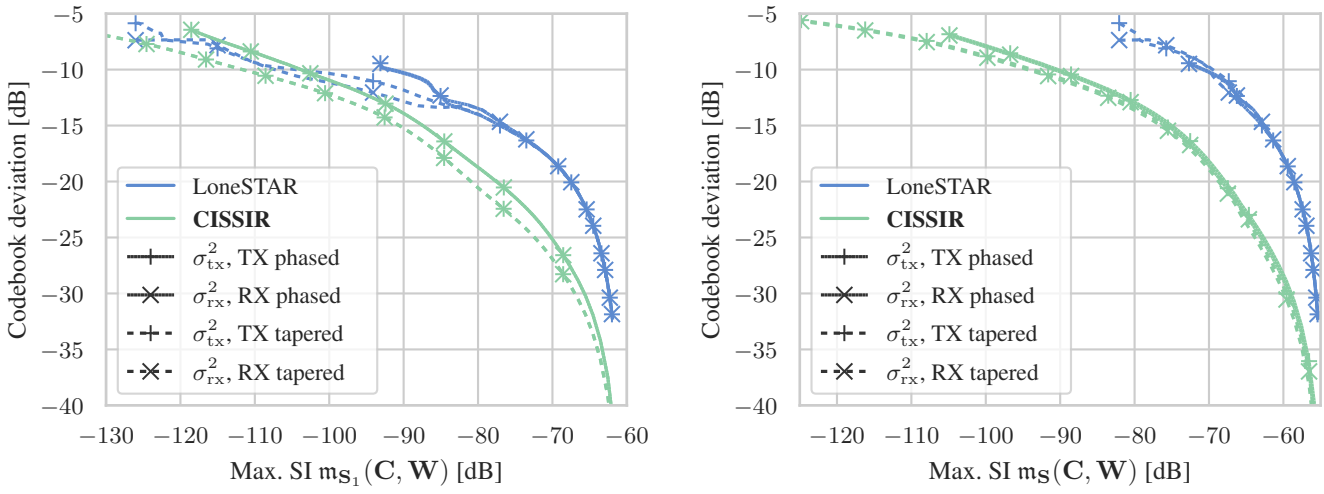
under per-antenna power constraints and a maximum codebook deviation $\sigma^2_{\text{cb}} \geq \max\{\sigma^2_{\text{tx}}, \sigma^2_{\text{rx}}\}$. The authors follow an alternating approach so that the TX codebook $\mathbf{W}$ is optimized first and then plugged in (29) for the optimization of the RX codebook $\mathbf{C}$. In addition to this, the codebooks are projected to their feasibility sets, $\mathcal{W} \ni \mathbf{W}$ and $\mathcal{C} \ni \mathbf{C}$, after the corresponding optimization step.

For a fair comparison, we first consider a simplified flat-fading SI model that only includes the direct coupling $\mathbf{S}_1(t)$, and we set $\bar{\mathbf{H}} = \mathbf{S}_1(\tau_1)$ in (29) for LoneSTAR optimization, with τ_1 the mean path delay. For CISSIR, we simply set $\mathbf{S}(t) = \mathbf{S}_1(\tau_1)\delta(t-\tau_1)$ in Algorithms 1–2.

We optimize LoneSTAR and CISSIR for different values of σ^2_{cb} and target SI ε, respectively, and plot the resulting trade-off curves in Fig. 6a, assuming either phased or tapered arrays. Here, we observe that CISSIR can reduce SI further than LoneSTAR for the same σ^2_{tx} and σ^2_{rx}, with a max. SI gap going up to 14 dB for a codebook deviation around -18 dB. We suppose this performance gap lies on LoneSTAR's beam-exhaustive SI sum-power minimization, via (29), which is sensible for full-duplex communication but overly conservative for ISAC, as per Lemma 1. An additional trade-off analysis using (29) instead of $\mathfrak{m}_{\mathbf{S}_1}(\mathbf{C},\mathbf{W})$ seems to confirm this supposition, as it displays an SI sum-power up to 5 dB lower for LoneSTAR than for CISSIR.

In Fig. 6a, CISSIR reaches around 2 dB more SI-reduction with tapered $(\mathcal{W}_\triangleright, \mathcal{C}_\triangleright)$ than with phased arrays $(\mathcal{W}_\oslash, \mathcal{C}_\oslash)$ for the same deviation, which is expected since $\mathcal{W}_\oslash \subset \mathcal{W}_\triangleright$ and $\mathcal{C}_\oslash \subset \mathcal{C}_\triangleright$. For LoneSTAR, tapering allows for more SI reduction, but it performs similarly to phased arrays for max. SI over -85 dB, perhaps due to the considered per-antenna power constraint [17]. CISSIR curves coincide for TX and RX, which is expected for $\beta = 1$. In fact, a different choice of $\beta > 0$ would simply alter the parameter $\epsilon \in \{\varepsilon\beta, \varepsilon\beta^{-1}\}$ in Problem (11), causing a mere horizontal curve shift along the max. SI axis.

We plot the trade-off curves again for our full multipath SI model $\mathbf{S}(t)$ in Fig. 6b. Since LoneSTAR only considers flat-frequency SI, we retain the $\mathbf{S}_1(t)$-optimized LoneSTAR codebooks above to evaluate their performance under multipath SI. Unsurprisingly, LoneSTAR experiences a performance degradation in this multipath scenario, as it is unable to attain a max. SI below -83 dB. On the other hand, CISSIR can still reduce the max. SI well below -100 dB and -120 dB for phased and tapered arrays, respectively. While the authors in [17] do not directly address multipath channels, we should note that LoneSTAR could be extended with time-domain filtering or covariance-based modeling to capture such effects.



(a) Single-path SI channel $\mathbf{S}_1(t)$.

(b) Multipath SI channel $\mathbf{S}(t)$.

Fig. 6. TX and RX codebook deviations σ^2_{tx} and σ^2_{rx} as functions of the max. SI for LoneSTAR and CISSIR, both for phased and tapered arrays.

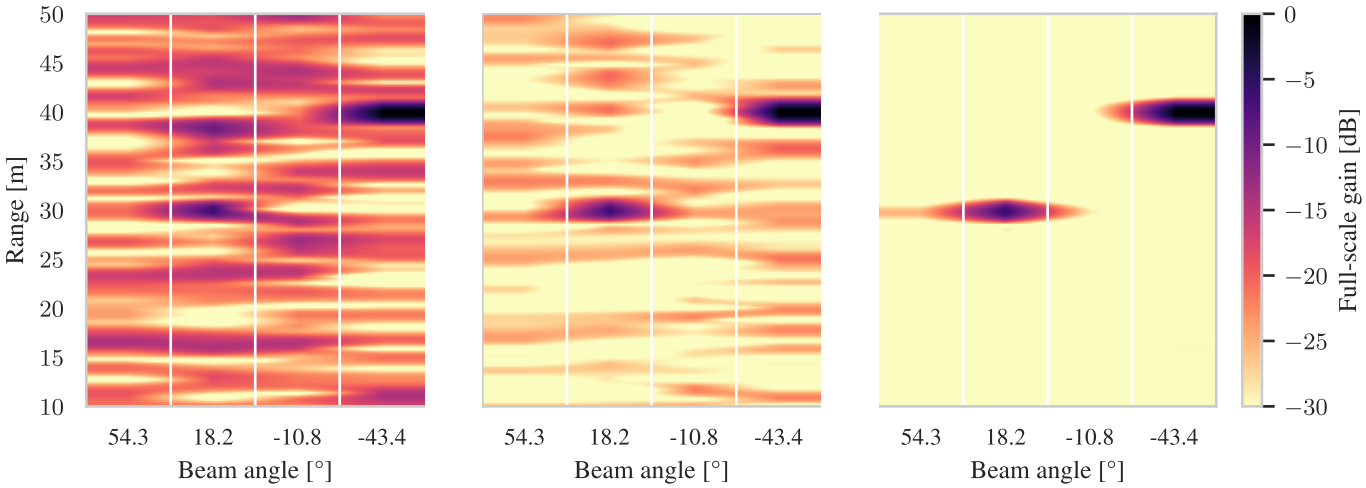
Overall, CISSIR performs better than LoneSTAR in terms of the max. SI. In order to demonstrate once again this metric's relevance for ISAC under hybrid beamforming, we compute range-angle maps with $L = K = 4$ orthogonal beams in Fig. 7, and we compare LoneSTAR and CISSIR codebooks for $\sigma^2_{\mathrm{tx}} \approx -18.2\,\mathrm{dB}$ and a single-path SI channel. Here, we add a second target at 30 m and 20°, and we cancel the residual SI digitally [11] after ADC sampling. Despite this digital SI cancellation, we observe a higher noise floor for LoneSTAR in Fig. 7a than for CISSIR in Fig. 7b, as a result of the greater $\mathfrak{m}_{\mathbf{S}_1}(\mathbf{C},\mathbf{W})$ and the ADC's limited dynamic range.

D. Algorithmic performance

We finalize our investigation with some empirical results on the time complexity and feasibility of CISSIR, which we summarize in Table II.

To analyze time complexity, we report the first and third quartiles of the studied algorithms' runtime on an AMD Epyc 73F3 processor. Here, we can see that phased CISSIR is slower than LoneSTAR, which can be explained by the space lifting of the SDP problem; e.g., Algorithm 2 must optimize L' $N \times N$ matrices to retrieve the $N \times L'$-sized TX codebook. While slower than 1 s, the runtime of Algorithm 2 should represent a negligible overhead in a practical calibration scheme, since the coherence time of SI channels has been reported to be in the order of minutes, at least [17], [34]. On the other hand, tapered CISSIR is almost 200 times faster than its phased counterpart and up to 130 times faster than LoneSTAR, thanks to the semi-closed-form solution of Algorithm 1.

Regarding problem feasibility, we can compute the minimum feasible SI exactly for tapered CISSIR as $\min_{k,\ell}(\bar{\sigma}(\mathbf{b}_k,\mathbf{G}_{\mathrm{rx}})\bar{\sigma}(\mathbf{a}_\ell,\mathbf{G}_{\mathrm{tx}}))$ (cf. Proposition 2). For phased



(a) LoneSTAR, $\mathfrak{m}_{\mathbf{S}_1}(\mathbf{C},\mathbf{W}) = -69.9\,\mathrm{dB}$.

(b) CISSIR, $\mathfrak{m}_{\mathbf{S}_1}(\mathbf{C},\mathbf{W}) = -80.6\,\mathrm{dB}$.

(c) Ground truth ($\mathbf{A},\mathbf{B}$ without SI or quantization).

Fig. 7. Range-angle maps for $L = K = 4$ beams with different codebooks and digital residual SI cancellation. TX deviation $\sigma^2_{\mathrm{tx}} \approx -18.2\,\mathrm{dB}$ in Figs. 7a–7b.

TABLE II
ALGORITHMIC METRICS FOR LONESTAR (PHASED AND TAPERED) AND CISSIR

SI channel model	Optimization time (1st – 3rd quartiles)			Minimum feasible SI		Largest SI gap	
	LoneSTAR	Phased CISSIR	Tapered CISSIR	Phased CISSIR	Tapered CISSIR	Phased CISSIR	Tapered CISSIR
Single-path $\mathbf{S}_1(t)$	0.16 s–1.02 s	1.20 s–1.48 s	6.5 ms–7.7 ms	−123 dB	−165.4 dB	0.0 dB	0.5 dB
Multipath $\mathbf{S}(t)$	-	1.14 s–1.39 s	4.6 ms–8.2 ms	−108 dB	−132.1 dB	0.4 dB	1.9 dB

arrays, we estimate the minimum feasible SI as the target SI ε for which $\Upsilon(\tilde{\mathbf{Z}})$ in (17) is above 0.995 on average. In any case, we conclude that CISSIR provides optimal solutions in our scenarios for a wide range of ε, over 50 dB below the reference max. SI in Table I.

Finally, we note that the original SI constraint (7b) is fulfilled quite tightly in our simulations. In fact, the "SI gap" between max. SI $\mathfrak{m}_{\mathbf{S}}(\mathbf{C},\mathbf{W})$ and target SI ε is at most 0.4 dB for max. SI above −108 dB in our experiments, and it only increases to 2 dB for multipath tapered CISSIR when it approaches its feasible SI. For single-path SI, the observed gap is at most 0.5 dB, which seems to confirm the expected tightness of (9) for spatially sparse symmetric SI channels. Furthermore, we have noticed similar gaps for the saturation bound (23) in the context of Proposition 4. In conclusion, it can be argued that CISSIR is a valid approximation to the original Problem (7), based on the obtained SI gap values from Table II.

VI. CONCLUSION

In this paper, we have proposed codebooks with integral split for self-interference reduction (CISSIR) as an evolution of the existing beam codebooks in current mobile networks, both for hybrid and analog schemes. CISSIR achieves notable self-interference (SI) reduction and thus paves the way for integrated sensing and communication (ISAC) beyond 5G.

The proposed methodology allows a systematic optimization of phased-array and tapered beam codebooks via semidefinite programming and spectral decomposition, respectively. Our framework also provides performance guarantees regarding multipath SI impairments in the analog domain. Most notably, we have derived an analytical bound on the quantization noise at the analog-to-digital converter, and we have proved its practicality via sensing simulations. Moreover, our link-level results show how CISSIR can reduce SI with a small impact on 5G-NR-based communication. Contrary to other available SI-reduced beam codebooks, our proposed method has easily interpretable optimization parameters, and it outperforms said codebooks for relevant ISAC performance indicators.

Future research can introduce other practical aspects into our optimization framework, such as subarrays, SI channel estimation errors, or quantized beamforming. In doing so, we aim towards the hardware realization of a high dynamic-range 5G-NR ISAC proof of concept.

APPENDIX

A. Proof of Proposition 1 (max. SI gap)

To prove $\mathfrak{m}_{\mathbf{S}}(\mathbf{C},\mathbf{W}) \le \widehat{\mathfrak{m}}_{\mathbf{S}}(\mathbf{C},\mathbf{W})$ in Proposition 1, we use the SVD in Definition 1 to bound the argument inside $\mathfrak{m}_{\mathbf{S}}(\mathbf{C},\mathbf{W}) \coloneqq \max_{k\in[K'],\ell\in[L']} \int_0^{T_\mathrm{c}} \left|\mathbf{c}_k^{\mathsf{H}}\mathbf{S}(t)\mathbf{w}_\ell\right| dt$ as:

$$\begin{aligned}
&\int_0^{T_\mathrm{c}} \left|\mathbf{c}_k^{\mathsf{H}}\mathbf{S}(t)\mathbf{w}_\ell\right| dt = \int_0^{T_\mathrm{c}} \left|\mathbf{c}_k^{\mathsf{H}}\mathbf{U}_t\boldsymbol{\Sigma}_t^{1/2}\boldsymbol{\Sigma}_t^{1/2}\mathbf{V}_t^{\mathsf{H}}\mathbf{w}_\ell\right| dt \\
\le &\int_0^{T_\mathrm{c}} \left\|\boldsymbol{\Sigma}_t^{1/2}\mathbf{U}_t^{\mathsf{H}}\mathbf{c}_k\right\|_2 \left\|\boldsymbol{\Sigma}_t^{1/2}\mathbf{V}_t^{\mathsf{H}}\mathbf{w}_\ell\right\|_2 dt \\
\le &\sqrt{\int_0^{T_\mathrm{c}} \left\|\boldsymbol{\Sigma}_t^{1/2}\mathbf{U}_t^{\mathsf{H}}\mathbf{c}_k\right\|_2^2 dt \int_0^{T_\mathrm{c}} \left\|\boldsymbol{\Sigma}_t^{1/2}\mathbf{V}_t^{\mathsf{H}}\mathbf{w}_\ell\right\|_2^2 dt} \\
= &\sqrt{\int_0^{T_\mathrm{c}} \mathbf{c}_k^{\mathsf{H}}\mathbf{U}_t\boldsymbol{\Sigma}_t\mathbf{U}_t^{\mathsf{H}}\mathbf{c}_k\, dt \int_0^{T_\mathrm{c}} \mathbf{w}_\ell^{\mathsf{H}}\mathbf{V}_t\boldsymbol{\Sigma}_t\mathbf{V}_t^{\mathsf{H}}\mathbf{w}_\ell\, dt}\,,
\end{aligned}$$

where we have applied the Cauchy-Schwarz inequality twice, first in its vector and then in its integral form. The proof is completed by applying max over $k \in [K']$ and $\ell \in [L']$.

B. Proof of Proposition 2 (tapered beamforming solution)

We proof the optimality of $\mathbf{z}_\star \in \mathbb{C}^P$ in Proposition 2 by constructing $\mathbf{z}_\star$ such that it fulfills, together with certain dual variables $\mu, \lambda > 0$, the Karush–Kuhn–Tucker (KKT) conditions for the following convex relaxation of Problem (13)

$$\underset{\mathbf{z}\in\mathbb{C}^P}{\text{maximize}}\ \Re(\mathbf{r}^{\mathsf{H}}\mathbf{z}) \qquad \text{s.t.} \qquad \mathbf{z}^{\mathsf{H}}\mathbf{G}\mathbf{z} \le \epsilon, \quad \mathbf{z}^{\mathsf{H}}\mathbf{z} \le 1\,. \tag{30}$$

We note that Problem (30) fulfills Slater's condition, as $\mathbf{0}$ is an interior point of the problem's feasible region. Consequently, strong duality holds and thus any point satisfying the KKT conditions is optimal.

First, we recall the KKT stationarity condition as $\nabla\mathcal{L}(\mathbf{z}_\star,\mu,\lambda) = \mathbf{0}$ for the Lagrangian of (30):

$$\mathcal{L}(\mathbf{z},\mu,\lambda) = -\Re(\mathbf{r}^{\mathsf{H}}\mathbf{z}) + \mu\left(\mathbf{z}^{\mathsf{H}}\mathbf{G}\mathbf{z} - \epsilon\right) + \lambda\left(\mathbf{z}^{\mathsf{H}}\mathbf{z} - 1\right),$$

from which it follows that[3]

$$\begin{aligned}
-\mathbf{r} + 2\mu\mathbf{G}\mathbf{z}_\star + 2\lambda\mathbf{z}_\star = \mathbf{0} \ \Rightarrow\ \mathbf{z}_\star &= \frac{1}{2}\left(\mu\mathbf{G} + \lambda\mathbf{I}\right)^{-1}\mathbf{r} = \\
&\eta\left(\mathbf{Q}\boldsymbol{\Gamma}\mathbf{Q}^{\mathsf{H}} + \nu\mathbf{I}\right)^{-1}\mathbf{r} = \eta\mathbf{Q}\underbrace{\left(\boldsymbol{\Gamma} + \nu\mathbf{I}\right)^{-1}}_{=:\mathbf{D}_\nu}\mathbf{Q}^{\mathsf{H}}\mathbf{r}\,,
\end{aligned} \tag{31}$$

where we have applied the spectral decomposition of $\mathbf{G} = \mathbf{Q}\boldsymbol{\Gamma}\mathbf{Q}^{\mathsf{H}}$ and the variable changes $\eta = 1/2\mu$ and $\nu = \lambda/\mu$ for $\mu, \lambda, \eta, \nu > 0$. Notice that $\mathbf{z}_\star$ is obtained by multiplying $\mathbf{r}$ with the positive definite matrix $\mathbf{Q}\mathbf{D}_\nu\mathbf{Q}^{\mathsf{H}}$, and scaling by η to ensure $\|\mathbf{z}_\star\|_2 = 1$.

Since we are searching for strictly positive dual variables, $\mathbf{z}_\star$ should satisfy all constraints in (13) and (30) with equality to fulfill complementary slackness, i.e.:

$$\begin{aligned}
1 = \mathbf{z}_\star^{\mathsf{H}}\mathbf{z}_\star &= \eta\mathbf{r}^{\mathsf{H}}\mathbf{Q}\mathbf{D}_\nu\mathbf{Q}^{\mathsf{H}}\mathbf{Q}\mathbf{D}_\nu\mathbf{Q}^{\mathsf{H}}\mathbf{r}\eta = \eta^2\mathbf{r}^{\mathsf{H}}\mathbf{Q}\mathbf{D}_\nu^2\mathbf{Q}^{\mathsf{H}}\mathbf{r}\,, \\
\epsilon = \mathbf{z}_\star^{\mathsf{H}}\mathbf{G}\mathbf{z}_\star &= \eta\mathbf{r}^{\mathsf{H}}\mathbf{Q}\mathbf{D}_\nu\mathbf{Q}^{\mathsf{H}}\mathbf{Q}\boldsymbol{\Gamma}\mathbf{Q}^{\mathsf{H}}\mathbf{Q}\mathbf{D}_\nu\mathbf{Q}^{\mathsf{H}}\mathbf{r}\eta \\
&= \eta^2\mathbf{r}^{\mathsf{H}}\mathbf{Q}\mathbf{D}_\nu\boldsymbol{\Gamma}\mathbf{D}_\nu\mathbf{Q}^{\mathsf{H}}\mathbf{r}\,,
\end{aligned} \tag{32}$$

[3]Formally, (31) follows from the stationarity condition for a reformulation of Problem (30) with real optimization variables, cf. [30, Equation (2)].

and if we divide both expressions by $\eta^2 > 0$, we obtain:

$$\mathbf{r}^{\mathsf{H}}\mathbf{Q}\mathbf{D}_\nu\mathbf{\Gamma}\mathbf{D}_\nu\mathbf{Q}^{\mathsf{H}}\mathbf{r} = \frac{\epsilon}{\eta^2} = \epsilon\,\mathbf{r}^{\mathsf{H}}\mathbf{Q}\mathbf{D}_\nu^2\mathbf{Q}^{\mathsf{H}}\mathbf{r}$$
$$\sum_{p=1}^{P}\frac{\sigma_p\left|\mathbf{q}_p^{\mathsf{H}}\mathbf{r}\right|^2}{\left(\sigma_p+\nu\right)^2} = \epsilon\sum_{p=1}^{P}\frac{\left|\mathbf{q}_p^{\mathsf{H}}\mathbf{r}\right|^2}{\left(\sigma_p+\nu\right)^2}\,, \tag{33}$$

where we have used the diagonality of $\mathbf{D}_\nu$ and $\mathbf{\Gamma}$ to write out the matrix multiplications. We can now multiply both sides of (33) by $\prod_{p=1}^{P}\left(\sigma_p+\nu\right)^2 > 0$, and rearrange to obtain $\mathcal{P}(\nu) = 0$. Hence, if $\mathcal{P}(\nu)$ has a positive root $\nu_\star$, the KKT conditions of (30) are fulfilled for $\mathbf{z}_\star$, as given in Proposition 2, with

$$\mu = \frac{1}{2\eta} = \frac{1}{2}\sqrt{\mathbf{r}^{\mathsf{H}}\mathbf{Q}\mathbf{D}_{\nu_\star}^2\mathbf{Q}^{\mathsf{H}}\mathbf{r}} > 0\,, \quad \text{and} \quad \lambda = \nu_\star\mu > 0\,.$$

More specifically, (μ, λ) are dual feasible, stationarity is fulfilled by (31), and (32) ensures both complementary slackness and primal feasibility. Moreover, $\mathbf{z}_\star$ is also feasible for (13) by (32), and thus (30) becomes a tight convex relaxation of (13). The following Lemma 2 completes the proof by guaranteeing the existence of $\nu_\star > 0$ under the conditions of Proposition 2.

Lemma 2. *Consider $\mathbf{G} = \mathbf{Q}\mathbf{\Gamma}\mathbf{Q}^{\mathsf{H}} \in \mathbb{S}_+^P$, $\{\sigma_p\}_{p=1}^P$, $\mathbf{r} \in \mathcal{Z}$, and $\epsilon > 0$ as defined in Proposition 2. Any of the conditions i) and ii) therein are sufficient for the existence of a positive root for*

$$\mathcal{P}(\nu) \coloneqq \sum_{p=1}^{P}\left(\sigma_p-\epsilon\right)\left|\mathbf{q}_p^{\mathsf{H}}\mathbf{r}\right|^2\prod_{q\neq p}\left(\sigma_q+\nu\right)^2.$$

Proof. From Descartes' rule of signs [42], the existence of a positive root $\nu_\star > 0$ for $\mathcal{P}(\nu)$ is given by the sufficient but not necessary condition that $\mathcal{P}(\nu)$ has nonzero highest- and lowest-degree coefficients with opposite signs.

Under either condition i) or ii), we have $\epsilon < \mathbf{r}^{\mathsf{H}}\mathbf{G}\mathbf{r}$, and thus the highest-degree coefficient c_{2P-2} is positive:

$$\begin{aligned} c_{2P-2} &= \sum_{p=1}^{P}\left(\sigma_p-\epsilon\right)\left|\mathbf{q}_p^{\mathsf{H}}\mathbf{r}\right|^2 \\ &= \mathbf{r}^{\mathsf{H}}\sum_{p=1}^{P}\sigma_p\mathbf{q}_p\mathbf{q}_p^{\mathsf{H}}\mathbf{r} - \epsilon\mathbf{r}^{\mathsf{H}}\mathbf{Q}\mathbf{Q}^{\mathsf{H}}\mathbf{r} \\ &= \mathbf{r}^{\mathsf{H}}\mathbf{G}\mathbf{r} - \epsilon\mathbf{r}^{\mathsf{H}}\mathbf{r} = \mathbf{r}^{\mathsf{H}}\mathbf{G}\mathbf{r} - \epsilon > 0\,. \end{aligned}$$

For the lowest-degree coefficient, we need to consider the rank of $\mathbf{G}$. For the rank-deficient $\mathbf{G}$ in i), it can be proven by mathematical evaluation that the lowest nonzero coefficient has degree $2R-2$, with $R = P - \operatorname{rank}(\mathbf{G}) > 0$ and $R < P$, and that it equals

$$c_{2R-2} = -\epsilon\sum_{p:\,\sigma_p=0}\left|\mathbf{q}_p^{\mathsf{H}}\mathbf{r}\right|^2\prod_{\sigma_q\neq 0}\sigma_q^2 < 0\,.$$

Therefore, $\mathcal{P}(\nu)$ always has a positive root $\nu_\star$ for $\operatorname{rank}(\mathbf{G}) \in [1,\, P-1]$ and $\epsilon \in (0, \mathbf{r}^{\mathsf{H}}\mathbf{G}\mathbf{r})$, as given by condition i) in Proposition 2.

If $\mathbf{G}$ is full rank, then $(\forall\, p \in [P])\ \sigma_p > 0$, and the existence of $\nu_\star > 0$ is guaranteed by $\epsilon < \mathbf{r}^{\mathsf{H}}\mathbf{G}\mathbf{r}$ and

$$c_0 = \sum_{p=1}^{P}\left(\sigma_p-\epsilon\right)\left|\mathbf{q}_p^{\mathsf{H}}\mathbf{r}\right|^2\prod_{q\neq p}\sigma_q^2 < 0$$
$$\sum_{p=1}^{P}\frac{\left(\sigma_p-\epsilon\right)\left|\mathbf{q}_p^{\mathsf{H}}\mathbf{r}\right|^2}{\sigma_p^2} < 0$$
$$\bar{\sigma}(\mathbf{r},\mathbf{G}) = \frac{\sum_{p=1}^{P}\left|\mathbf{q}_p^{\mathsf{H}}\mathbf{r}\right|^2/\sigma_p}{\sum_{p=1}^{P}\left|\mathbf{q}_p^{\mathsf{H}}\mathbf{r}\right|^2/\sigma_p^2} < \epsilon\,,$$

as stated in condition ii). □

C. Proof of Lemma 1 (quantization noise bound)

The total noise variance for $\hat{\mathbf{y}}[i]$ in (22) can be rewritten as

$$\begin{aligned} \mathbb{E}\left[\left\|\hat{\mathbf{y}}[i]-\mathbf{y}(iT_{\mathrm{S}})\right\|_2^2\right] &= \mathbb{E}\left[\sum_{k=1}^{K}\left|\hat{y}_k[i]-y_k(iT_{\mathrm{S}})\right|^2\right] \\ = \sum_{k=1}^{K}\mathbb{E}[|v_k[i]+u_k[i]|^2] &\overset{\text{a)}}{=} \sum_{k=1}^{K}\mathbb{E}[|v_k[i]|^2] + \mathbb{E}[|u_k[i]|^2] \\ &= \sum_{k=1}^{K}\left(\sigma_{\mathrm{T}}^2+\sigma_{\mathrm{Q}}^2\right) \overset{\text{b)}}{=} K\sigma_{\mathrm{T}}^2 + K\mathfrak{b}_{\mathrm{Q}}y_{\mathrm{fs}}^2\,, \end{aligned} \tag{34}$$

where we have used a) the independence of $u_k[i]$ and $v_k[i]$, and b) the definition of σ_{Q}^2 in (18). Now, we turn our attention to y_{fs} in (19). Using the maximum norm $|\cdot|_\infty$, we note that

$$\begin{aligned} y_{\mathrm{fs}} &= \gamma\max_{k\in[K]}\left|\sum_{\ell=1}^{L}\left(\mathbf{c}_{\imath(k)}^{\mathsf{H}}\mathbf{S}\mathbf{w}_{\jmath(\ell)}\right)*x_\ell\right|_\infty \\ &\leq \gamma\max_{k'\in[K']}\left|\sum_{\ell=1}^{L}\left(\mathbf{c}_{k'}^{\mathsf{H}}\mathbf{S}\mathbf{w}_{\jmath(\ell)}\right)*x_\ell\right|_\infty, \end{aligned} \tag{35}$$

where we upper bound y_{fs} independently of $\imath$ by considering k' in the full codomain of $\imath$. For any $k' \in [K']$, we have:

$$\begin{aligned} &\left|\sum_{\ell=1}^{L}\left(\mathbf{c}_{k'}^{\mathsf{H}}\mathbf{S}\mathbf{w}_{\jmath(\ell)}\right)*x_\ell\right|_\infty \overset{\text{a)}}{\leq} \sum_{\ell=1}^{L}\left|\left(\mathbf{c}_{k'}^{\mathsf{H}}\mathbf{S}\mathbf{w}_{\jmath(\ell)}\right)*x_\ell\right|_\infty \overset{\text{b)}}{\leq} \\ &\sum_{\ell=1}^{L}\left|\mathbf{c}_{k'}^{\mathsf{H}}\mathbf{S}\mathbf{w}_{\jmath(\ell)}\right|_1|x_\ell|_\infty \leq \max_{\ell'\in[L']}\left|\mathbf{c}_{k'}^{\mathsf{H}}\mathbf{S}\mathbf{w}_{\ell'}\right|_1\sum_{\ell=1}^{L}|x_\ell|_\infty\,. \end{aligned} \tag{36}$$

In (36), a) follows from the triangular inequality, and b) from Young's convolution inequality. From (35) and (36), it follows

that

$$
\begin{aligned}
y_{\mathrm{fs}}^2 \leq & \gamma^2 \max_{k'\in[K'],\ell'\in[L']} \left|\mathbf{c}_{k'}^{\mathsf{H}}\mathbf{S}\mathbf{w}_{\ell'}\right|_1^2 \left(\sum_{\ell=1}^{L}|x_\ell|_\infty\right)^2 \overset{\text{a)}}{=} \\
& \gamma^2 \mathrm{m}_{\mathbf{S}}^2(\mathbf{C},\mathbf{W}) \left(\sum_{\ell=1}^{L}|x_\ell|_\infty\right)^2 \overset{\text{b)}}{=} \\
& \gamma^2 \mathrm{m}_{\mathbf{S}}^2(\mathbf{C},\mathbf{W}) \left(\sum_{\ell=1}^{L}|x_\ell|_2\sqrt{\rho_{x_\ell}/T}\right)^2 \overset{\text{c)}}{\leq} \\
& \gamma^2 \mathrm{m}_{\mathbf{S}}^2(\mathbf{C},\mathbf{W}) \sum_{\ell=1}^{L}|x_\ell|_2^2 \sum_{\ell=1}^{L}\rho_{x_\ell}/T \overset{\text{d)}}{=} \\
& \gamma^2 \mathrm{m}_{\mathbf{S}}^2(\mathbf{C},\mathbf{W}) P_{\mathrm{tx}} \sum_{\ell=1}^{L}\rho_{x_\ell}\,.
\end{aligned}
\tag{37}
$$

Here we have applied a) the definition of the max. SI in (5), b) the PAPR expression (21), c) the Cauchy-Schwarz inequality, and d) the power relation (20). The proof is completed by upper bounding y_{fs}^2 in (34) with the right-hand side of (37) and rearranging.

ACKNOWLEDGMENT

The authors of this work acknowledge the financial support by Germany's Federal Ministry for Research, Technology and Space (BMFTR) in the programme "Souverän. Digital. Vernetzt." Joint project 6G-RIC (grant numbers: 16KISK020K, 16KISK030). Rodrigo Hernangómez acknowledges BMFTR support in the project "KOMSENS-6G" (grant number: 16KISK121).

REFERENCES

[1] J. A. Zhang, M. L. Rahman, K. Wu, X. Huang, Y. J. Guo, S. Chen, and J. Yuan, "Enabling Joint Communication and Radar Sensing in Mobile Networks—A Survey," *IEEE Communications Surveys Tutorials*, vol. 24, no. 1, pp. 306–345, 2022.

[2] F. Liu, C. Masouros, A. P. Petropulu, H. Griffiths, and L. Hanzo, "Joint Radar and Communication Design: Applications, State-of-the-Art, and the Road Ahead," *IEEE Transactions on Communications*, vol. 68, no. 6, pp. 3834–3862, Jun. 2020.

[3] H. Wymeersch, A. Pärssinen, T. E. Abrudan, A. Wolfgang, K. Haneda, M. Sarajlic, M. E. Leinonen, M. F. Keskin, H. Chen, S. Lindberg, P. Kyösti, T. Svensson, and X. Yang, "6G Radio Requirements to Support Integrated Communication, Localization, and Sensing," in *2022 Joint European Conference on Networks and Communications & 6G Summit (EuCNC/6G Summit)*, Jun. 2022, pp. 463–469.

[4] F. Liu, Y. Cui, C. Masouros, J. Xu, T. X. Han, Y. C. Eldar, and S. Buzzi, "Integrated Sensing and Communications: Toward Dual-Functional Wireless Networks for 6G and Beyond," *IEEE Journal on Selected Areas in Communications*, vol. 40, no. 6, pp. 1728–1767, Jun. 2022.

[5] L. Giroto de Oliveira, B. Nuss, M. B. Alabd, A. Diewald, M. Pauli, and T. Zwick, "Joint Radar-Communication Systems: Modulation Schemes and System Design," *IEEE Transactions on Microwave Theory and Techniques*, vol. 70, no. 3, pp. 1521–1551, Mar. 2022.

[6] C. Baquero Barneto, T. Riihonen, M. Turunen, L. Anttila, M. Fleischer, K. Stadius, J. Ryynanen, and M. Valkama, "Full-Duplex OFDM Radar With LTE and 5G NR Waveforms: Challenges, Solutions, and Measurements," *IEEE Transactions on Microwave Theory and Techniques*, vol. 67, no. 10, pp. 4042–4054, Oct. 2019.

[7] T. Riihonen and K. E. Kolodziej, "Full-Duplex ISAC," in *Integrated Sensing and Communications*. Singapore: Springer Nature, 2023, pp. 537–565.

[8] J. Marin, M. Bernhardt, M. Heino, and T. Riihonen, "Monostatic FMCW Radar Architecture for Multifunction Full-Duplex Radios," in *2021 55th Asilomar Conference on Signals, Systems, and Computers*, Oct. 2021, pp. 640–644, iSSN: 2576-2303.

[9] M. A. Richards, J. A. Scheer, and W. A. Holm, *Principles of modern radar*. Raleigh (N.C.): Citeseer, 2010, vol. 1.

[10] Z. Xiao and Y. Zeng, "Waveform Design and Performance Analysis for Full-Duplex Integrated Sensing and Communication," *IEEE Journal on Selected Areas in Communications*, vol. 40, no. 6, pp. 1823–1837, Jun. 2022.

[11] G. C. Alexandropoulos, M. A. Islam, and B. Smida, "Full-Duplex Massive Multiple-Input, Multiple-Output Architectures: Recent Advances, Applications, and Future Directions," *IEEE Vehicular Technology Magazine*, vol. 17, no. 4, pp. 83–91, Dec. 2022.

[12] R. Askar and W. Keusgen, "Lossless Decoupling Networks for RF Self-Interference Cancellation in MIMO Full-Duplex Transceivers," *IEEE Journal on Selected Areas in Communications*, vol. 41, no. 9, pp. 2765–2779, Sep. 2023.

[13] M. T. Yalcinkaya, P. Sen, and G. Fettweis, "Comparative analysis of antenna isolation characteristic with & without self-interference reduction techniques towards in-band full-duplex operation," *IET Microwaves, Antennas & Propagation*, vol. 17, no. 5, pp. 329–342, 2023.

[14] K. E. Kolodziej, J. G. McMichael, and B. T. Perry, "Multitap RF Canceller for In-Band Full-Duplex Wireless Communications," *IEEE Transactions on Wireless Communications*, vol. 15, no. 6, pp. 4321–4334, Jun. 2016.

[15] A. Liu, T. Riihonen, and W. Sheng, "Full-Duplex Analog Beamforming Design for mm-Wave Integrated Sensing and Communication," in *2023 IEEE Radar Conference (RadarConf23)*, San Antonio, TX, USA, May 2023, pp. 1–6.

[16] R. Hernangómez, J. Fink, R. L. Cavalcante, Z. Utkovski, and S. Stańczak, "Optimized Detection with Analog Beamforming for Monostatic Integrated Sensing and Communication," in *ICC 2024 - IEEE International Conference on Communications*, Denver, CO, Jun. 2024, pp. 317–323.

[17] I. P. Roberts, S. Vishwanath, and J. G. Andrews, "LoneSTAR: Analog Beamforming Codebooks for Full-Duplex Millimeter Wave Systems," *IEEE Transactions on Wireless Communications*, vol. 22, no. 9, pp. 5754–5769, Sep. 2023.

[18] M. Bayraktar, C. Rusu, N. González-Prelcic, and H. Chen, "Self-Interference Aware Codebook Design for Full-Duplex Joint Sensing and Communication Systems at Mmwave," in *2023 IEEE 9th International Workshop on Computational Advances in Multi-Sensor Adaptive Processing (CAMSAP)*, Dec. 2023, pp. 231–235.

[19] M. Bayraktar, N. González-Prelcic, and H. Chen, "Hybrid Precoding and Combining for mmWave Full-Duplex Joint Radar and Communication Systems Under Self-Interference," in *ICC 2024 - IEEE International Conference on Communications*, Jun. 2024, pp. 915–920.

[20] Z. Liu, S. Aditya, H. Li, and B. Clerckx, "Joint Transmit and Receive Beamforming Design in Full-Duplex Integrated Sensing and Communications," *IEEE Journal on Selected Areas in Communications*, vol. 41, no. 9, pp. 2907–2919, Sep. 2023.

[21] Z. He, W. Xu, H. Shen, D. W. K. Ng, Y. C. Eldar, and X. You, "Full-Duplex Communication for ISAC: Joint Beamforming and Power Optimization," *IEEE Journal on Selected Areas in Communications*, vol. 41, no. 9, pp. 2920–2936, Sep. 2023.

[22] E. Tohidi, R. Askar, Z. Utkovski, and S. Stańczak, "Full-duplex operation of ISAC: Self-interference reduction from the lens of IRS," in *2023 IEEE Globecom Workshops (GC Wkshps)*. IEEE, 2023, pp. 1880–1885.

[23] B. Smida, G. C. Alexandropoulos, T. Riihonen, and M. A. Islam, "In-Band Full-Duplex Multiple-Input Multiple-Output Systems for Simultaneous Communications and Sensing: Challenges, methods, and future perspectives," *IEEE Signal Processing Magazine*, vol. 41, no. 5, pp. 8–16, Sep. 2024.

[24] E. Dahlman, S. Parkvall, and J. Skold, *5G NR: The Next Generation Wireless Access Technology*, 1st ed. London England ; San Diego, CA: Academic Press, Aug. 2018.

[25] X. Fu, D. Le Ruyet, R. Visoz, V. Ramireddy, M. Grossmann, M. Landmann, and W. Quiroga, "A Tutorial on Downlink Precoder Selection Strategies for 3GPP MIMO Codebooks," *IEEE Access*, vol. 11, pp. 138 897–138 922, 2023.

[26] R. M. Dreifuerst and R. W. Heath, "Massive MIMO in 5G: How Beamforming, Codebooks, and Feedback Enable Larger Arrays," *IEEE Communications Magazine*, vol. 61, no. 12, pp. 18–23, Dec. 2023.

[27] R. Askar, J. Chung, Z. Guo, H. Ko, W. Keusgen, and T. Haustein, "Interference Handling Challenges toward Full Duplex Evolution in

5G and Beyond Cellular Networks," *IEEE Wireless Communications*, vol. 28, no. 1, pp. 51–59, Feb. 2021.

[28] Y. He, X. Yin, and H. Chen, "Spatiotemporal characterization of self-interference channels for 60-GHz full-duplex communication," *IEEE Antennas and Wireless Propagation Letters*, vol. 16, pp. 2220–2223, 2017.

[29] S. Mandelli, M. Henninger, M. Bauhofer, and T. Wild, "Survey on Integrated Sensing and Communication Performance Modeling and Use Cases Feasibility," in *2023 2nd International Conference on 6G Networking (6GNet)*, Oct. 2023, pp. 1–8.

[30] B. Fuchs, "Application of Convex Relaxation to Array Synthesis Problems," *IEEE Transactions on Antennas and Propagation*, vol. 62, no. 2, pp. 634–640, Feb. 2014.

[31] J. Hoydis, S. Cammerer, F. A. Aoudia, A. Vem, N. Binder, G. Marcus, and A. Keller, "Sionna: An Open-Source Library for Next-Generation Physical Layer Research," *arXiv preprint*, 2022, arXiv:2203.11854 [cs].

[32] S. Diamond and S. Boyd, "CVXPY: A Python-embedded modeling language for convex optimization," *Journal of Machine Learning Research*, vol. 17, no. 83, pp. 1–5, 2016.

[33] T. Wild, A. Grudnitsky, S. Mandelli, M. Henninger, J. Guan, and F. Schaich, "6G Integrated Sensing and Communication: From Vision to Realization," in *2023 20th European Radar Conference (EuRAD)*, Sep. 2023, pp. 355–358.

[34] I. P. Roberts, A. Chopra, T. Novlan, S. Vishwanath, and J. G. Andrews, "Beamformed Self-Interference Measurements at 28 GHz: Spatial Insights and Angular Spread," *IEEE Transactions on Wireless Communications*, vol. 21, no. 11, pp. 9744–9760, Nov. 2022.

[35] S. Boyd and L. Vandenberghe, *Convex optimization*. Cambridge University Press, 2004.

[36] G. Sagnol, "A class of semidefinite programs with rank-one solutions," *Linear Algebra and its Applications*, vol. 435, no. 6, pp. 1446–1463, Sep. 2011.

[37] R. Gray, "Quantization noise spectra," *IEEE Transactions on Information Theory*, vol. 36, no. 6, pp. 1220–1244, Nov. 1990.

[38] E. Hewitt and K. A. Ross, *Abstract Harmonic Analysis: Volume I: Structure of Topological Groups Integration Theory Group Representations*. Springer Science & Business Media, Dec. 2012.

[39] 3GPP, "Study on channel model for frequencies from 0.5 to 100 GHz," TR 38.901, Release 16.1, Nov. 2020.

[40] D. Dehghani, "Analog Beamforming Simulations for Self-Interference Cancellation in Integrated Sensing and Communication," Master's thesis, Karlsruhe Institute of Technology, Karlsruhe, Germany, Jun. 2024.

[41] 3GPP, "NR; Physical layer procedures for data," TS 38.214, Release 16.5, Apr. 2021.

[42] X. Wang, "A Simple Proof of Descartes's Rule of Signs," *The American Mathematical Monthly*, vol. 111, no. 6, pp. 525–526, Jun. 2004.